

Comparative Design, Scaling, and Control of Appendages for Inertial Reorientation

Thomas Libby, *Student Member, IEEE*, Aaron M. Johnson, *Member, IEEE*, Evan Chang-Siu, *Member, IEEE*, Robert J. Full, and Daniel E. Koditschek, *Fellow, IEEE*

Abstract—This paper develops a comparative framework for the design of actuated inertial appendages for planar aerial reorientation. We define the inertial reorientation template, the simplest model of this behavior, and leverage its linear dynamics to reveal the design constraints linking a task with the body designs capable of completing it. As practicable inertial appendage designs lead to morphology that is generally more complex, we advance a notion of “anchoring,” whereby a judicious choice of physical design in concert with an appropriate control policy yields a system whose closed-loop dynamics are sufficiently captured by the template to permit all further designs to take place in its far simpler parameter space. This approach is effective and accurate over the diverse design spaces afforded by existing platforms, enabling a performance comparison through the shared task space. We analyze examples from the literature and find advantages to each body type, but conclude that tails provide the highest potential performance for reasonable designs. Thus motivated, we build a physical example by retrofitting a tail to a RHex robot and present empirical evidence of its efficacy.

Index Terms—Biologically inspired robots, legged robots, mechanism design, motor selection, tails.

I. INTRODUCTION

TAILS and tail-like appendages have shown promise to greatly enhance robot agility, enabling such feats as aerial reorientation [1]–[3], hairpin turns [4]–[6], and disturbance rejection [7]–[9]. These behaviors are examples of inertial reorientation (IR), whereby internal configuration adjustments generate inertial forces that control the body’s orientation. The stabilizing function of inertial appendages appears to be important to

Manuscript received November 17, 2015; revised May 7, 2016; accepted June 16, 2016. Date of publication September 7, 2016; date of current version December 2, 2016. This paper was recommended for publication by Associate Editor R. Carloni and Editor P. Dupont upon evaluation of the reviewers’ comments. This work was supported in part by the ARL/GDRS RCTA and in part by the National Science Foundation under the CIBER-IGERT Award DGE-0903711 and the CABI-R Award CDI-II 1028237. Portions of this work (including some experimental results) previously appeared in [1].

T. Libby is with the Departments of Mechanical Engineering and Integrative Biology, University of California Berkeley, Berkeley, CA 94720 USA (e-mail: tlibby@berkeley.edu).

A. M. Johnson is with the Department of Mechanical Engineering, Carnegie Mellon University, Pittsburgh, PA 15232 USA (e-mail: amj1@andrew.cmu.edu).

E. Chang-Siu is with the Department of Engineering Technology, California State University Maritime Academy, Vallejo, CA 94590 USA (e-mail: echangsiu@csum.edu).

R. J. Full is with the Department of Integrative Biology, University of California Berkeley, Berkeley, CA 94720 USA (e-mail: rjfull@berkeley.edu).

D. E. Koditschek is with the Department of Electrical and Systems Engineering, University of Pennsylvania, Philadelphia, PA 19104 USA (e-mail: kod@seas.upenn.edu).

Color versions of one or more of the figures in this paper are available online at <http://ieeexplore.ieee.org>.

Digital Object Identifier 10.1109/TRO.2016.2597316

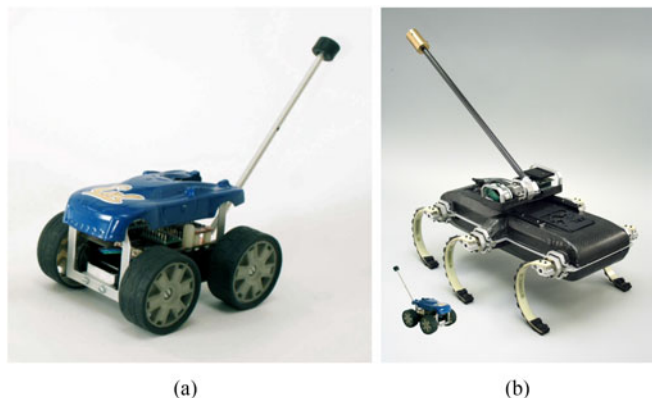


Fig. 1. (a) Tailbot [2], [17] and (b) RHex [10], [11] with a new tail, and with an approximately sized image of Tailbot inserted.

animals across a wide variety of behaviors and size scales, suggesting that this mechanism could be broadly useful for robotic systems such as the small wheeled Tailbot [2] [see Fig. 1(a)] or the larger legged RHex [10], [11] [see Fig. 1(b)]. While tails may be the most conspicuous example of IR morphology, any internal movement of mass can induce rotation in a body. Animals also use the inertia of their legs [12], [13], wings [14], or spine [15] to accomplish similar behaviors and engineered systems use radially symmetric wheels inside satellites or on terrestrial vehicles [16].

This paper presents a formal framework for the selection and comparison of robot bodies that are capable of a planar, aerial, IR task. Design of the morphology for a dynamic behavior like IR is a persistently challenging problem in robotics, since task completion must be enforced over the full design space through the execution of a hybrid and possibly nonlinear dynamical system. We propose a reductionist approach, collapsing the complexity of the variously possible body plans to a far simpler model whose dynamics we can solve. The task-feasible set of this simple model, together with its generic controller, is then pulled back through this “morphological reduction” to specify the more complex design. We use this framework to evaluate the merits of a range of possible morphologies, and to design a new tail for the RHex robot [see Fig. 1(b)], documenting its efficacy for recovery from otherwise injurious falls, as illustrated in Figs. 7 and 9.

A. Prior Work

The study of IR dates to the 19th century “falling cat problem” [15]. More recent studies show that by swinging their tails, lizards can self-right in less than a body length [18], re-

orient through zero net angular momentum IR maneuvers [19], and control their attitude in leaps [17]. To the authors’ best knowledge, the first robot to utilize an inertial tail is the Uniroo, a one-leg hopper that stabilized its body pitch in part with an actuated tail [20]. Other early robotic tails were passive or slowly actuated and used to maintain contact forces while climbing vertical surfaces [21], [22]. The idea of using a robot’s existing limbs as tail-like appendages was first explored as a method of “legless locomotion” [23].

The effectiveness of the IR capabilities in lizards inspired the creation of Tailbot [see Fig. 1(a)], a robot with an active tail that enabled disturbance regulation [17], air-righting, and traversing rough terrain [2]. Since Tailbot, there has been an explosion in the number of robotic tails for reorientation [3]–[6], [24] and stabilization [7]–[9], [25], [26] in both aerial and terrestrial domains. Noninertial tails have also seen continued interest with tails that affect the body through substrate interaction [27]–[29] and aerodynamics [30], [31]. Recently, other morphologies have also been explored including two-degree-of-freedom (DOF) tails that greatly expand the range of possible motions [9], [25], [32] and flailing limbs that reuse existing appendages [33]. Many of these robots draw their inspiration from a diverse variety of animals, including moths [24], [34], seahorses [35], kangaroos [9], cheetahs [6], [7], [26], and even dinosaurs [17], [36]. The growing interest in robotic IR appendages demonstrates the potential benefits of inertial forces and motivates the need for truly comparative design methodologies.

B. Paper Outline and Contributions

To instantiate the appendage design problem, in this work, we consider an aerial IR self-righting task. While the machines examined in this paper are nominally terrestrial locomotors, their rapid dynamic behavior includes leaps, falls, and other short aerial phases where their limbs cannot provide control authority through ground reaction forces. We will restrict motion in both the templates and anchors to a 2-D plane, in the absence of external forces. The task is defined as a finite-time zero angular momentum reorientation: a rotation of the body configuration θ_b from initial condition $\theta_b(0) = \dot{\theta}_b(0) = 0$, to rest at some final angle $\theta_{b,f}$ in a desired time t_f . That is

$$\theta_b(t_f) - \theta_{b,f} = 0, \quad \dot{\theta}_b(t_f) = 0. \quad (1)$$

Because any internal motion—whether a rotation of tails, wheels, limbs, or even body bending—must yield some IR in flight, we need a method of directly comparing the performance and design merits of a diverse array of potential body structures. The simplicity of the shared underlying behavior is suggestive of a template [37], or simplest model, whose tractable dynamics yield a compact description of the relationship between morphology and task performance. We present the IR template (see Section II-A) and solve its simple dynamics (see Section II-B) relative to the task (1) (see Section II-C), revealing the constraints linking that task with the set of body designs capable of completing it. We then refine that set by reducing it to the

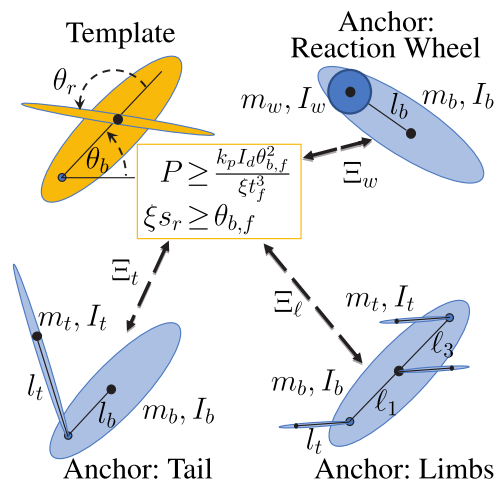


Fig. 2. The IR template is a planar two-link model parameterized in part by power P , effectiveness ξ , appendage stroke s_r , and driven inertia I_d ; designs satisfying the constraints are feasible with respect to the task [see (1)]. More complex IR bodies (anchors) may be designed or compared through the template by mapping their physical parameters to those of the template, using a morphological reduction Ξ_i , as summarized in Table II.

instances where the control and gearing are optimal for the assigned task (see Section II-D).

The embodiment of this simple template in a more complex model of real morphology (an anchor, [37])¹ provides for a shared parameterization of IR efficacy. This is a new idea that enables the design and direct comparison of different candidate bodies through a generalized template–anchor relationship that we now briefly describe intuitively before charting its technical development in this paper and in Appendix A. Whereas in this problem the template DOFs typically embed naturally into those of the morphologies, the same is not true of their respective design parameters. Thus, our agenda of reusably “anchoring” a template design in a variety of bodies requires a new mapping between their parameter spaces. Beyond the specifics of the task, one of the central contributions of this paper is to articulate and formalize the role of this morphological reduction. As we detail in Section III, mapping the design parameters (mass, length, and inertia) of a detailed model down to the simpler template parameters carries a pullback of the simple template controller back up to the anchor as well.

We define anchor models for tails (see Section III-A), reaction wheels (see Section III-B), and synchronized groups of limbs (hereafter termed “flails”; see Section III-C), and propose morphological reductions from their respective parameter spaces to the parameter space of the template (summarized in Fig. 2 and Table II). We use these morphological reductions to find evidence of similar template–anchor relationships in design examples from a dozen different platforms (see Section IV-A), which exhibit close (or in some cases exact) kinematic and dynamic approximations (depicted in Fig. 5). The reductions afford a perfor-

¹Here, there is no time-asymptotic specification and, therefore, no attracting invariant set as achieved empirically, e.g., in [10] and [38], and formally as well, e.g., in [39]. Instead, we observe that the anchors manifest a close approximation to the template over large interesting regions of parameter spaces (see Appendix A).

mance comparison of each morphology (see Section IV-B), and a more general comparative scaling analysis (see Section IV-C).

We assess anecdotally the utility of our design framework in three ways. First, we use our design specification to analyze the tail added to a RHex hexapedal robot [10] (specifically X-RHex Lite, XRL [11]; see Fig. 1(b) and Section V-A1). Second, we use the common IR template to compare the RHex tailed-body instantiation with a limbed-body instantiation using only RHex's legs (see Section V-A2). Finally, we present empirical results (see Section V-B) that illustrate the manner in which IR behaviors can help robots perform high-performance potentially injurious aerial reorientation using inertial limbs.

In the interest of space and clarity, we have omitted the more lengthy derivations required to reach some expressions in this paper; the full derivations can be found in the accompanying technical report [40].

II. TEMPLATE BEHAVIOR

This section develops the simplest IR model and solves its dynamics explicitly in the context of the task specification. From this, we derive two constraints specifying the feasible portion of parameter space, over which the robot design may be optimized (or—more practicably—“toleranced,” as we exemplify in Section V) to best meet performance needs outside the reorientation task. To this end, we define the IR template (depicted in Fig. 2) as a planar system comprised of two rigid bodies—an “appendage” and a “body” pinned at their shared centers of mass (COMs). A motor applies a torque acting on θ_r , the internal angle between the bodies, and can steer θ_b , the orientation of the body, through the action of a controller. We will thus choose (θ_r, θ_b) as our generalized coordinates. The appendage moment of inertia (MOI), I_a , and the template body MOI, I_d , specify the passive mechanics.

The template's behavior during the reorientation task is fully parameterized by a combination of its physical (body) parameters, powertrain, and control parameters, and its task specification, defined throughout the rest of this section and summarized in Table I as

$$\mathbf{p} = [\xi, I_d, s_r, P, \omega_m, t_s, \theta_{b,f}, t_f] \in \mathcal{P}. \quad (2)$$

Not all parameter sets \mathbf{p} are self-consistent, as clearly only certain bodies are capable of completing a given task. The remainder of this section will be dedicated to finding a parameterization of the constraints defining the feasible subset of parameters $\mathcal{R} \subset \mathcal{P}$. Any parameter set in \mathcal{R} is “task-worthy” in the sense that its physical parameters enable completion of its task description. The “task-worthy” set will be used to solve two design problems.

P1 Body selection: The task specification is fixed at the outset, and the other parameters are chosen to satisfy its completion.

P2 Performance evaluation: The physical parameters are fixed, and given t_f and $\theta_{b,f}$ are queried against a resulting feasible set.

We next derive the kinematics and dynamics of this IR template model and then solve those dynamics in normalized form to reveal the feasible set \mathcal{R} .

TABLE I
KEY SYMBOLS USED THROUGHOUT THIS PAPER WITH SECTION OR EQUATION NUMBER OF THE INTRODUCTION MARKED

g_h, g_θ	Time and angle functions (9), (10)
$\bar{g}_h, \bar{g}_\theta, \bar{g}_c$	Normalized time and angle functions (15), (16), (18)
H_O	Angular momentum (3)
I_a, I_b, I_t	Inertia of the appendage, body, and tail (Sections II-A and III-A)
$I_d, I_{d,t}$	Driven inertia of the template and tail (Section II-B), (42)–(44)
l_b, l_t	Length from the pivot to the body and tail (Section III-A)
k_p, k_t, k_s	Power, time, and speed constants (23), (Section II-C2)
l_i	Limb offsets (Section III-C)
L	Characteristic body length (Section IV-C)
m_b, m_t	Mass of the body and tail (Section III-A)
m_r	Reduced mass (31)
N	Number of limbs (Section III-C)
$\mathbf{p} \in \mathcal{P}$	Template parameters (2)
$\mathbf{p}_i \in \mathcal{P}_i$	Anchor i parameters (29), (47), (50)
P	Motor power (Section II-B)
$\mathcal{R}, \mathcal{R}^*, \mathcal{R}_i$	Allowable parameter set (12), (26), (28)
s_r	Range of motion (Section II-A)
t, t_s, t_h, t_f	Time, switching, halting and final time (Sections II-A and II-C1)
$\bar{t}, \bar{t}_s, \bar{t}_c, \bar{t}_h$	Normalized, switching, critical, and halting time (Section II-C1)
γ	Time scaling parameter (14)
η	Nonlinearity parameter (33)
$\theta_b, \theta_t, \theta_r, \theta_h$	Body, tail, relative, and halting appendage angles (Section II-A)
$\bar{\theta}$	Normalized relative angle (Section II-C1)
ξ, ξ_t	Effectiveness of the template and tail (4), (32)
ξ_w, ξ_t	Effectiveness of the reaction wheel, and limbs (48), (53)
Ξ_i	Morphological reduction i (27)
τ	Motor torque (Section II-B)
$\omega_m, \bar{\omega}_m$	Motor and normalized no-load speed (Sections II-B and II-C1)

A. Template Kinematics

For a planar single-DOF IR system in free fall, the rotation available in the body's workspace is limited by the capacity for internal motion. To derive a functional relationship between the (internal) shape angular velocity and the (external) body orientation velocity, we will use the nonholonomic constraint resulting from conservation of the system's total angular momentum. From any point O , Euler's laws for a rigid body state that $\dot{\mathbf{H}}_O = \mathbf{M}_O$, where \mathbf{H}_O is the total angular momentum about O , and \mathbf{M}_O is the net moment about O . For short aerial behaviors in robots larger than a few grams, we will assume that the external forces and torques (particularly aerodynamic torques) are negligible so that $\mathbf{M}_O = 0$, and hence, total angular momentum about O is conserved.

The template's angular momentum about the perpendicular axis (\mathbf{E}_3) of its COM

$$H_O = (I_a + I_d)\dot{\theta}_b + I_a\dot{\theta}_r \quad (3)$$

where $H_O \mathbf{E}_3 := \mathbf{H}_O$, and $\dot{\theta}_b$ and $\dot{\theta}_r$ are derivatives with respect to time t . Normalizing by the total MOI, $I_a + I_d$, and solving for body angular velocity reveals that the template kinematics are parameterized by a single dimensionless constant ξ , the effectiveness of the IR template²

$$\dot{\theta}_b = \tilde{H}_O - \xi\dot{\theta}_r, \quad \xi := \frac{I_a}{I_a + I_d} \quad (4)$$

²Note that this quantity differs from that of [1], wherein effectiveness ε was defined as the ratio of link velocities.

where \tilde{H}_O is the normalized system angular momentum. Hence, the angular velocity of the body can be decomposed into two physically interesting components: a drift term influenced solely by external impulses, and the velocity induced by internal shape change that has been called the local connection vector field [41] (hereafter connection field, although note that in this transient setting, there is no cyclic shape change). This equation directly governs performance in two distinct tasks: 1) orientation regulation after an impulse, where the task is to maintain a stable body angle ($\dot{\theta}_b = 0$), with a relative velocity $\dot{\theta}_r = \tilde{H}_O/\xi$; and 2) zero angular momentum reorientation ($H_O = 0$), where the task is to change the body orientation to some angle $\theta_{b,f}$ in t_f seconds [see (1)], given the constraint of the connection field, $\dot{\theta}_b = -\xi\dot{\theta}_r$.

In the latter case, body rotation is directly a function of appendage rotation. Under the assumption that $\dot{\theta}_r$ is positive

$$\dot{\theta}_b = \frac{d\theta_b}{dt} = \frac{\partial\theta_b}{\partial\theta_r} \frac{d\theta_r}{dt} = -\xi\dot{\theta}_r, \quad \frac{\partial\theta_b}{\partial\theta_r} = -\xi \quad (5)$$

expressing the 1-D connection field that reveals the constant differential relationship between internal and external rotation.³ For this template, the connection field is constant and equal to $-\xi$. The body stroke is directly proportional to appendage stroke, and hence, a limit s_r on the range of motion of the appendage will limit the achievable body rotation.

B. Template Dynamics

A real terrestrial robot is constrained by the duration of its aerial phase (fall, leap, or other dynamic behavior), and this imposes a new set of requirements on the parameters that specify the actuation. This section characterizes the behavior of a conventionally power-limited actuation scheme and defines a controller for that actuator.

1) *Newtonian and Actuator Dynamics*: As the template consists of two rigid bodies pinned through their concentric COMs, derivation of the equations of motion is trivial—the angular acceleration of body and tail is opposite in sign and equal to the motor torque normalized by each body’s MOI. Since the tail angle is kinematically related to that of the body by (5), we will simply consider the body dynamics

$$\ddot{\theta}_b = \frac{\tau}{I_d} \quad (6)$$

where τ is the motor torque. The ratio of joint torque to body angular acceleration is equal to the body’s MOI in the template, I_d , but is more complex in the anchors (coupling appendage masses, etc.); to avoid confusion with the inertia of the physical body segment in the anchor models, we will call this ratio the “driven” inertia.

To capture the essential limitation of any powertrain in a time-sensitive task—the rate at which it can change the mechanical energy of the driven system—we augment the template’s dynamics with a simple piecewise-linear actuator model, in which torque falls linearly with increasing speed (we extend this to allow for current limits in Appendix C). This model is not only a

good approximation of a DC motor [42], but is general enough to capture to first order the effort–flow relationships of many other speed-dependent actuators including biological muscles [43]. The maximum available actuator torque depends on activation (terminal voltage, $V = \pm V_m$, for some maximum voltage V_m) and speed

$$\tau(V, \dot{\theta}_r) = \begin{cases} \text{sgn}(V) \tau_m \left(1 - \frac{|\dot{\theta}_r|}{\omega_m}\right), & V\dot{\theta}_r < 0 \\ \text{sgn}(V) \tau_m, & V\dot{\theta}_r \geq 0 \end{cases} \quad (7)$$

where τ_m is the stall torque and ω_m is the no-load speed of the motor after the gearbox (and hence the no-load speed of the appendage relative to the body).

Since we seek to specify the entire powertrain, we find it convenient to decouple the roles of the actuator and the transmission by parameterization with respect to peak mechanical power $P = \tau_m \omega_m / 4$ (whose product form cancels the appearance of the gear ratio) and drivetrain no-load speed ω_m (whose linear dependence upon the gear ratio makes it a useful surrogate for the transmission). The required gear ratio of a physical gearbox or other transmission is then the ratio of ω_m to the motor’s actual no-load speed.

2) *Controller Design*: Notwithstanding the voluminous literature on time-optimal control in mechatronics and robotics settings (e.g., along specified paths [44] and exposing actuator dynamics [45]), we have not been able to find a formal treatment of the robust minimum time problem for our simple hybrid motor model (7). Therefore, we will take the naïve approach and embrace a single-switch open-loop bang–bang controller as offering the simplest and most paradigmatic expression of “fast repositioning” for a (back EMF perturbed) double integrator [46]. We relax the bang–bang controller assumption in Appendix B and, in particular, show that a proportional-derivative (PD) feedback controller closely and robustly approximates (and given high enough gains, converges to) the open-loop control policy. We further verify this in the empirical results (see Section V-B), which use a PD controller to approximate the bang–bang controller.

The bang–bang control strategy makes a single switch between the acceleration and braking dynamics at a time t_s , such that the body comes to a halt at the desired final orientation $\theta_{b,f}$.⁴ During the single-switch reorientation from $\theta_b = 0$, the body will accelerate from rest and brake to the final angle $\theta_b = \theta_{b,f}$ with no overshoot, with $\dot{\theta}_b \geq 0$ and $\dot{\theta}_r \leq 0$ for the entire maneuver. Using (5), the torque can be rewritten to eliminate the dependence on θ_r . The hybrid dynamics are described by an acceleration phase and a braking phase

$$\ddot{\theta}_b = \begin{cases} \frac{4P}{\omega_m I_d} \left(1 - \frac{\dot{\theta}_b}{\xi \omega_m}\right), & \text{for } 0 \leq t < t_s \\ -\frac{4P}{\omega_m I_d}, & \text{for } t \geq t_s. \end{cases} \quad (8)$$

⁴This may be replaced by an event-based guard condition $G(\theta_b, \dot{\theta}_b) = 0$, as derived in [40, Sec. II-A].

³In the anchor models, this relationship may be nonlinear or nonmonotonic.

3) *Behavior in Reorientation Task*: Based on this template kinematics, dynamics, and controller structure, we now examine the resulting behavior of the system in this reorientation task. First, note that due to local integrability of the nonholonomic constraint [see (5)], the system has only a single DOF after the initial conditions are chosen. We, therefore, choose to define the initial conditions as $\theta_r = \theta_b := 0$ and express the dynamics only in terms of θ_b . The system starts at rest so that $\dot{\theta}_b = 0$. We can write the system behavior in closed form by integrating the linear switched dynamics in (8) from this initial condition until the body again comes to a halt at a time t_h . See [40, Sec. I] for details on this integration. The halting time can be written as an explicit function of the template parameters [see (2)]

$$t_h = g_h(\mathbf{p}) := t_s + \frac{I_d \xi \omega_m^2}{4P} \left(1 - \exp \left(-\frac{4P}{I_d \xi \omega_m^2} t_s \right) \right) \quad (9)$$

along with the final angle $\theta_b = \theta_h$

$$\theta_h = g_\theta(\mathbf{p}) := \xi \omega_m t_s - \frac{I_d \xi^2 \omega_m^3}{8P} \left(1 - \exp \left(-\frac{8P}{I_d \xi \omega_m^2} t_s \right) \right). \quad (10)$$

C. Dynamical Task Encoding

The physical relationships derived in the previous two sections enable a straightforward representation of the task-feasible parameter subset \mathcal{R} containing all self-consistent parameter sets. This restricted set can be written as a system of constraints to facilitate the two design problems identified at the beginning of this section: P1 (body selection), in which the task specification (t_f and $\theta_{b,f}$) is fixed at the outset and \mathcal{R} prescribes the corresponding feasible body designs; and P2 (performance evaluation), where the achievable task set is identified, given a fixed body design (values of ξ , I_d , P , ω_m , s_r , and t_s).

The first constraint arises from the kinematic relation (5) and ensures that the rotation by the task, $\theta_{b,f}$, falls within any physical constraints on rotation. If the design has a finite range of motion s_r (so that $\theta_r \in [0, s_r]$), then any design meeting the task specification (1) must satisfy

$$\xi s_r \geq \theta_{b,f}. \quad (11)$$

Obviously, bodies with unlimited range of motion satisfy this constraint trivially. The second constraint ensures that the halting time [see (9)] falls within the task completion time t_f . The third constraint ensures that the body, under the bang–bang controller (parameterized by t_s) [see (10)], stops at the correct angle. Taken together, these constraints define \mathcal{R} as

$$\mathcal{R} := \left\{ \mathbf{p} \in \mathcal{P} \mid \xi s_r \geq \theta_{b,f}, t_f \geq g_h(\mathbf{p}), \theta_{b,f} = g_\theta(\mathbf{p}) \right\}. \quad (12)$$

For the body selection problem P1, any design, $\mathbf{p} \in \mathcal{R}$, satisfying these constraints is “task-worthy” in that its physical and controller parameters satisfy its task specification. The performance evaluation problem P2 is also easily specified using this representation: fixing all parameters save t_f and $\theta_{b,f}$ specifies

a 2-D subspace of achievable tasks (see Fig. 6 for a graphical example).⁵

Unfortunately, \mathcal{R} still leaves many DOFs for task-worthy designs for the body selection design problem. In the remainder of this section, we show that the gearing and control parameters (ω_m and t_s , respectively) can be eliminated through optimization, thereby enabling a more compact and considerably more prescriptive set.

1) *Spatiotemporally Normalized Template Behavior*: The isolation of the effect of gearing and control on \mathcal{R} is complicated by their nonlinear interaction with the other dimensioned parameters in \mathbf{p} . To remove the effect of scale and expose these relationships, we will nondimensionalize (9) and (10), seeking a spatiotemporal rescaling⁶ parameterized by γ , such that

$$\tilde{t}_s = \gamma t_s, \quad \tilde{t}_f = \gamma t_f, \quad \tilde{t}_h = \gamma t_h, \quad \tilde{\theta}_h = \frac{\theta_h}{\theta_{b,f}} \quad (13)$$

where $\tilde{\cdot}$ indicates dimensionless values. We find that choosing

$$\gamma := \left(\frac{4P\xi}{I_d \theta_{b,f}^2} \right)^{\frac{1}{3}} \quad (14)$$

enables a particularly convenient reduction of g_h and g_θ [see (9) and (10)], written as a function of only two normalized parameters

$$\tilde{t}_h = \tilde{g}_h(\tilde{\omega}_m, \tilde{t}_s) := \tilde{t}_s + \tilde{\omega}_m^2 \left(1 - \exp \left(\frac{-\tilde{t}_s}{\tilde{\omega}_m^2} \right) \right) \quad (15)$$

$$\tilde{\theta}_h = \tilde{g}_\theta(\tilde{\omega}_m, \tilde{t}_s) := \tilde{\omega}_m \tilde{t}_s - \frac{\tilde{\omega}_m^3}{2} \left(1 - \exp \left(\frac{-2\tilde{t}_s}{\tilde{\omega}_m^2} \right) \right) \quad (16)$$

where $\tilde{\omega}_m$ is a dimensionless actuator parameter that stands as a proxy for gearing

$$\tilde{\omega}_m := \frac{\xi \omega_m}{\gamma \theta_{b,f}}. \quad (17)$$

In the rescaled coordinates, the reorientation task requires that the system halts at $\tilde{\theta}_h = 1$, constraining the normalized parameters to one DOF. This freedom can be parameterized by $\tilde{\omega}_m$ through the implicit function specifying the “critical” switching time \tilde{t}_c , satisfying $\tilde{g}_\theta(\tilde{t}_c, \tilde{\omega}_m) = 1$ for a given choice of no-load speed

$$\tilde{t}_c = \tilde{g}_c(\tilde{\omega}_m) := \inf \{ \tilde{t}_s > 0 \mid \tilde{g}_\theta(\tilde{t}_s, \tilde{\omega}_m) = 1 \}. \quad (18)$$

When the other system parameters are chosen, the designer can choose the controller that completes the task by setting

$$t_s = \gamma \tilde{g}_c \left(\frac{\xi \omega_m}{\gamma \theta_{b,f}} \right) \quad (19)$$

automatically satisfying (and therefore obviating the need for) the third constraint in (12). With this choice, the scaled halting time depends only on the scaled no-load speed

$$\tilde{t}_h = \tilde{g}_h(\tilde{\omega}_m, \tilde{g}_c(\tilde{\omega}_m)). \quad (20)$$

⁵The largest task set will be found by allowing the switching time to vary with the task [i.e., using the third constraint in (12) to select t_s for each $\theta_{b,f}$].

⁶This rescaling can also be seen as a nondimensionalization of the template dynamics resulting in a normalized hybrid system that simplifies the integration of the dynamics; see [40, Sec. I].

The second constraint in (12) can now be written in a more useful form. The temporal demands of the task require that full template parameters [see (2)] be chosen so that the spatiotemporal rescaling meets the task specification. In particular, the value of γ [see (14)] (chosen through the selection of physical parameters) must ensure that the physical halting time meets the constraint

$$t_f \geq t_h = \frac{1}{\gamma} \tilde{t}_h = \frac{1}{\gamma} \tilde{g}_h(\tilde{\omega}_m, \tilde{g}_c(\tilde{\omega}_m)). \quad (21)$$

Substituting the definition of γ and rearranging terms yields a more compact version of the time constraint in (12), predicated on critical switching time

$$\frac{\xi P}{I_d} \geq k_p \frac{\theta_{b,f}^2}{t_f^3} \quad (22)$$

where k_p is a function of dimensionless gear ratio defined as

$$k_p := \frac{1}{4} \tilde{g}_h^3 \left(\frac{\xi \omega_m}{\gamma \theta_{b,f}}, \tilde{g}_c \left(\frac{\xi \omega_m}{\gamma \theta_{b,f}} \right) \right). \quad (23)$$

For a fixed task specification with a given inertia, power and effectiveness trade off directly. The value of k_p increases the requirements on P and ξ ; thus, k_p may be considered a performance ‘‘cost’’ imposed by suboptimal gearing. We will consider this cost when selecting an actuator design for RHex in Section V.

2) *Optimal Control and Gearing for the Template*: The gearing that maximizes performance in the critically switched task minimizes k_p or, equivalently, the dimensionless completion time t_h

$$\underset{\tilde{\omega}_m}{\text{minimize}} \quad \tilde{t}_h = \tilde{g}_h(\tilde{\omega}_m, \tilde{g}_c(\tilde{\omega}_m)). \quad (24)$$

This problem has a (numerically determined) unique global minimum at

$$\tilde{\omega}_m^* \approx 0.74 \quad (25)$$

corresponding to a minimal final dimensionless time $\tilde{t}_h^* := \tilde{g}_h(\tilde{g}_c(\tilde{\omega}_m^*), \tilde{\omega}_m^*) \approx 2.14$ [see Fig. 3(top)]. With this optimal $\tilde{\omega}_m^*$, we can find the minimal $k_p^* := \tilde{g}_h^3(\tilde{\omega}_m^*, \tilde{g}_c(\tilde{\omega}_m^*)) / 4 \approx 2.46$, corresponding to the minimal power requirement for (22). Similarly, the critical switching time at this optimum [see (18)] is a constant $k_t^* := \tilde{g}_c(\tilde{\omega}_m^*) \approx 1.62$. Finally, the optimal dimensioned no-load speed ω_m can be found from (17) and (21) as $\omega_m = k_s \theta_{b,f} / \xi t_f$, for $k_s := \tilde{\omega}_m^* \tilde{g}_h(\tilde{\omega}_m^*, \tilde{g}_c(\tilde{\omega}_m^*))$ (where, with these optimal values, $k_s^* \approx 1.58$).

This optimal bang–bang control can be expressed via the ratio $\tilde{t}_s / \tilde{t}_h$ [see Fig. 3(bottom)]; the optimized maneuver consists of full positive voltage for 76% of the total time, followed by full negative voltage until the body comes to a halt (see Fig. 4).

The designer seeking the optimally geared body for a critically switched reorientation task can then consider a refinement to \mathcal{R} [see (12)] that explicitly slaves two of the parameters

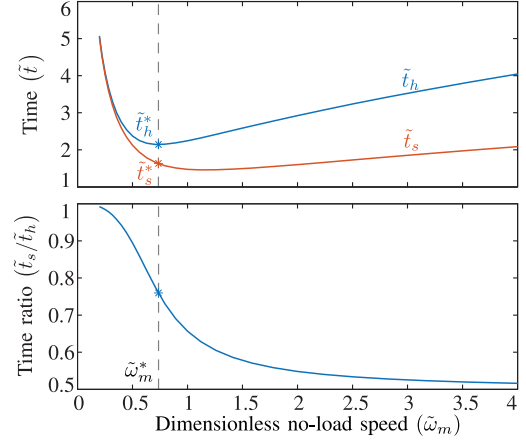


Fig. 3. Dimensionless system dynamics. Final time is globally minimized by $\tilde{\omega}_m^* \approx 0.74$ (top). Bang–bang control depends on $\tilde{\omega}_m$; at minimum final time, voltage switches at $\approx 76\%$ of final time.

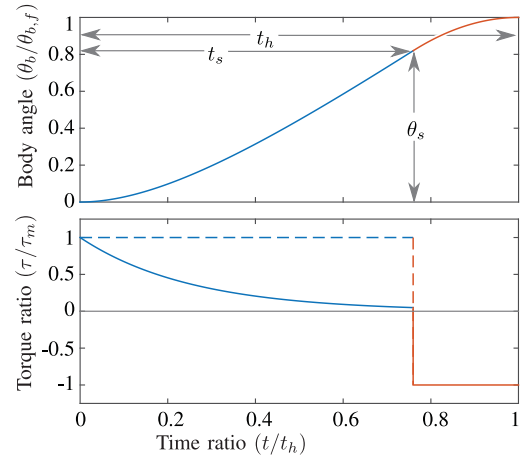


Fig. 4. (Top) System kinematics. (Bottom) Bang–bang control for optimal gearing selects maximal forward input (dashed line) for 76% of final time and, then, switches to full reverse; actual torque (solid line) is limited by back EMF during acceleration (blue) and current during braking (red).

(ω_m and t_s) to the others

$$\mathcal{R}^* := \left\{ \mathbf{p} \in \mathcal{P} \mid \xi s_r \geq \theta_{b,f}, \quad \frac{\xi P}{I_d} \geq \frac{k_p^* \theta_{b,f}^2}{t_f^3}, \right. \\ \left. \omega_m = k_s^* \frac{\theta_{b,f}}{\xi t_f}, \quad t_s = k_t^* \left(\frac{4P\xi}{I_d \theta_{b,f}^2} \right)^{\frac{1}{3}} \right\}. \quad (26)$$

D. Summary of Template Design Freedom

The solution of the template’s kinematics and dynamics enabled two representations of the task-feasible subset of design parameters, each serving a particular role in the two design problems specified at the beginning of this section. Starting with a fixed task specification (t_s and $\theta_{b,f}$), the body selection problem P1 can be summarized as a choice of the body parameters (ξ , I_d , s_r , and P) subject to the set constraint \mathcal{R}^* [see (26)], with the control and gearing (ω_m and t_s) selected optimally

TABLE II
MORPHOLOGICAL REDUCTIONS FOR THREE CANDIDATE ANCHORING BODIES

Attribute	Tail	Reaction wheel	Limbs
Inertial effectiveness, $\Xi_{i,\xi}$	$\frac{I_t + m_r l_t^2}{I_t + I_b + m_r (l_t^2 + l_b^2)}$	$\frac{I_w}{I_w + I_b + m_r l_b^2}$	$\frac{N(I_t + m_k l_t^2)}{I_b + m_t \sum_{i=1}^N \ell_i^2 + N(I_t + m_k l_t^2)}$
Driven inertia, Ξ_{i,I_d}	$(I_b + m_r l_b^2)(1 - \frac{2\eta}{\pi})$	$I_b + m_r l_b^2$	$I_b + m_t \sum_{i=1}^N \ell_i^2$
Anchoring accuracy ⁹	Approximate	Exact	Exact

based on this design. Alternatively, given an existing (or putative) design, the set \mathcal{R} [see (12)] can be used in a performance evaluation problem P2, specifying the achievable tasks. In this latter case, the “cost” of suboptimality can be computed using k_p [see (23)], or by finding an empirical k_p by substituting the template parameters into (22).⁷

III. ANCHORING VIA MORPHOLOGICAL REDUCTION

The concentrically pinned appendage of the template is not likely to exactly model practical physical designs, raising the question of how the template parameterization relates to real bodies available to a robot designer. We now explore how the task-feasible restriction on template parameters \mathcal{R} in (12) [or with optimized gearing and switching time \mathcal{R}^* in (26)] is reflected in the physical parameters (length, mass, and inertia) of bodies a designer might select for IR. A particular template instantiation $\mathbf{p} \in \mathcal{P}$ could be embodied in myriad ways. This paper considers three categories of physical IR morphologies that have appeared in the literature: tails, radially symmetric reaction wheels, and coordinated flailing limbs, with respective design spaces, \mathcal{P}_t , \mathcal{P}_w , and \mathcal{P}_ℓ . While the physical parameters and dynamics for these systems differ considerably, they all share the same configuration space and (scalar) control input space.⁸ Therefore, the state and input spaces can be mapped from template to anchor trivially, and we focus our attention on the problem of the parameter spaces. In this section, we show that these bodies can be put into formal correspondence with the template task representation by the introduction of a mapping from these spaces to that of the template

$$\Xi_i : \mathcal{P}_i \rightarrow \mathcal{P} \quad (27)$$

for $i \in \{t, w, \ell\}$, hereafter termed a morphological reduction.

The morphological reduction affords designers of these bodies the same insight achieved for templates. The “pullback” of the feasible set of body and task parameters through these maps yields an anchoring design in the sense of guaranteeing task achievement over the entire inverse image

$$\mathbf{p}_i \in \mathcal{R}_i := \Xi_i^{-1}(\mathcal{R}) \subset \mathcal{P}_i \quad (28)$$

[or similarly, $\mathcal{R}_i^* := \Xi_i^{-1}(\mathcal{R}^*)$]. The body selection and performance evaluation problems of the previous section can be

⁷A submaximal limit on torque, or suboptimal controllers like the PD scheme discussed earlier, also manifests as an increase in k_p .

⁸The limbed body is, of course, intrinsically possessed of higher DOF. Here, we consider only the case where a coordinating controller has rendered its input and state spaces identical to the template. See Appendix A for a full treatment of this anchoring.

expressed in the anchor’s task-feasible space \mathcal{R}_i by fixing either the task parameters or body parameters, respectively. We will employ both methods to explore reorientation morphology on RHex in Section V.

The kinematics and dynamics of anchors may deviate from that of the template, introducing nonlinearities and configuration dependence into the relationships corresponding to those derived in Section II. For these systems, the morphological reduction is an approximation, with error that varies with task specification and morphology.⁹

For the physical bodies discussed in this paper, the parameters defining the powertrain (P , ω_m , s_r), control (t_s), and task (t_f , $\theta_{b,f}$) have direct correspondences in both the template and anchor design spaces; thus, those components of Ξ are simply the identity map, and we use the same notation to describe these quantities in both template and anchor. However, equivalent parameters for effectiveness and inertia are not obvious *a priori* and, therefore, are the focus of the following sections (as summarized in Table II and Fig. 2). As shorthand for these nontrivial components of Ξ , we use $\Xi_{i,\xi}$ and Ξ_{i,I_d} to denote the canonical projection of Ξ_i onto ξ and I_d , respectively.

A. Tailed Morphological Reduction

Within this paper, we refer to any single mass-offset appendage specialized for IR as a “tail” (in contrast with flywheels and limbs, described below), although this configuration could also represent a two-segment body with an actuated spine [11], [47]. As in the template, the tailed system consists of two rigid bodies and one internal DOF, but in this case, the mass centers of the bodies are offset from the joint by some distance (l_b and l_t , for body and tail, respectively), and the derivation of the connection field is considerably more involved. The full parameter set for a tailed body motion is

$$\mathbf{p}_t := [m_b, I_b, l_b, m_t, I_t, l_t, s_r, P, \omega_m, t_s, \theta_{b,f}, t_f] \quad (29)$$

that is, mass, inertia, and COM distance from pivot for each of body and tail (see Fig. 2), as well as the appendage stroke, actuator power, no-load speed, controller switching time, and task specification.

1) *Tailed Body Kinematics*: The magnitude of the angular momentum about the system COM is nonlinearly configuration

⁹As shown in this section, the tail anchoring is exact when $l_b = 0$, the wheel anchoring is always exact, and the limb anchoring is exact only for the symmetry conditions described in Section III-C.

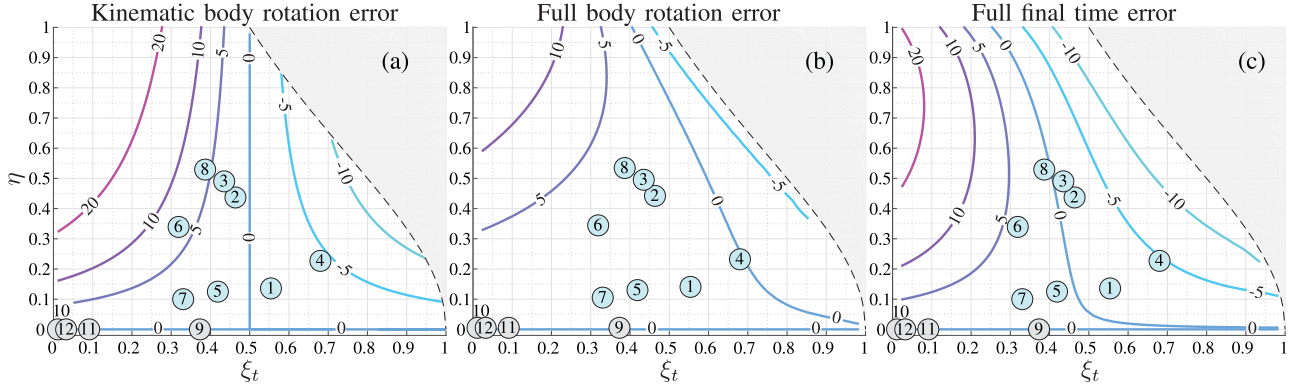


Fig. 5. Percent errors of approximation for tailed systems undergoing a half tail rotation centered around $\theta_r = 180^\circ$. Numbered points in gray and blue correspond to examples listed in Tables III and IV, respectively. Percent error in (a) body rotation due to effectiveness approximation $\eta = 0$ [level sets of (37)]. (b) Dimensionless final body rotation due to template optimization [level sets of (45)]. (c) Final time due to template optimization [level sets of (46)]. Note that for the full body and time error, all examples lie within 5% error.

dependent (see [40, Sec. III] for the full derivation)

$$H_{O,t} = (I_b + I_t + m_r(l_b^2 + l_t^2 - 2l_b l_t \cos \theta_r))\dot{\theta}_b + (I_t + m_r(l_t^2 - l_b l_t \cos \theta_r))\dot{\theta}_r \quad (30)$$

where

$$m_r := \frac{m_b m_t}{(m_b + m_t)} \quad (31)$$

is known as the reduced mass. As in (4), normalize the angular momentum by the total MOI¹⁰ about the COM, $I_b + I_t + m_r(l_t^2 + l_b^2)$, and define two dimensionless parameters—an equivalent effectiveness

$$\xi_t := \frac{I_t + m_r l_t^2}{I_t + I_b + m_r(l_t^2 + l_b^2)} \quad (32)$$

and a nonlinearity parameter

$$\eta := \frac{m_r l_b l_t}{I_t + m_r l_t^2}. \quad (33)$$

The normalized angular momentum is thus

$$\tilde{H}_{O,t} = (1 - 2\xi_t \eta \cos \theta_r)\dot{\theta}_b + \xi_t(1 - \eta \cos \theta_r)\dot{\theta}_r. \quad (34)$$

The second dimensionless constant η captures the extent to which the system deviates from the linear behavior of the template. Only a subset of the dimensionless parameter space is physically realizable because of coupling between the dimensionless constants and the requirement of nonnegativity of the dimensioned parameters (see [40, Sec. III-A]). The unreachable region is shaded gray in Fig. 5.

As in (5), setting $\tilde{H}_{O,t} = 0$ and applying the chain rule yields the connection field for the tail anchor

$$\frac{\partial \theta_b}{\partial \theta_r}(\theta_r) = -\xi_t \frac{1 - \eta \cos \theta_r}{1 - 2\xi_t \eta \cos \theta_r}. \quad (35)$$

Note that $\partial \theta_b / \partial \theta_r = -\xi_t = \text{const}$ when $\eta = 0$ or when $\xi_t = 0.5$, and note that the denominator is nonzero when $2\xi_t \eta < 1$,

¹⁰The total MOI for a general tail is configuration dependent; we take the MOI at $\theta_r = \pm 90^\circ$ to achieve the compact form presented here.

which is always true for physically realizable parameters (again, see [40, Sec. III-A]). When $\eta > 1$, the sign of the connection may change over the tail's range of motion so that transiently both tail and body rotate in the same direction.

Note that the kinematics are completely described by the connection field, and therefore, two systems with the same ξ_t and η have equal rotations of the body for any given tail rotation. Thus, tradeoffs in the physical parameters ($m_b, I_b, l_b, m_t, I_t, l_t$) that leave the dimensionless parameters (ξ_t, η) unchanged have no effect on the kinematics of the system. In terms of the physical parameters of a robot and tail, this 1-D connection field is

$$\frac{\partial \theta_b}{\partial \theta_r}(\theta_r) = -\frac{I_t + m_r(l_t^2 - l_b l_t \cos \theta_r)}{I_b + I_t + m_r(l_t^2 + l_b^2 - 2l_b l_t \cos \theta_r)}. \quad (36)$$

This quantity is at most unity (when the tail is infinitely long or heavy) and varies over both the configuration space of the robot and its design space.

For tails pivoting directly at the body COM, $l_b = 0$, the nonlinear terms vanish as $\eta = 0$, and the tail anchors to the template without error via equivalent effectiveness ξ_t . In general, the connection is not constant and the anchoring is approximate; this can be accomplished in a number of ways. The simplest approach (used for the rest of this paper) is to assume negligible effect of nonlinearity, i.e., $\eta \approx 0$, and simply choose $\Xi_{t,\xi}(\mathbf{p}_t) := \xi_t$ as in the body-centered case. This choice of (approximate) morphological reduction is not unique and may not be the most accurate in all situations, but it works well for all tailed robots described in Table IV. One alternative is to assume a small range of motion and evaluate the connection field at an intermediate value, such as $\Xi_{t,\xi}(\mathbf{p}_t) = \partial \theta_b / \partial \theta_r(180^\circ) = \xi_t(1 + \eta)/(1 + 2\xi_t \eta)$. The most accurate approximation for large tail swings is the average value over the full tail stroke (which can be found by integration of the connection field, as shown in [40, Sec. III-B]). This can be found in closed form, but the equation's complexity makes it cumbersome as a design tool, although useful for calculating or reducing error for a finalized design.

The relative error in body rotation over a sweep of the tail due to this approximation is plotted in Fig. 5(a) as

$$e_c(\xi_t, \eta) := \frac{\theta_{b,f} - \xi_t s_r}{\theta_{b,f}} \quad (37)$$

where the exact final body orientation is found by integrating the connection (36) over the tail sweep; an analytic expression for this function is derived in [40, Sec. III-B]. For robots with $\eta \approx 0$ or with $\xi_t \approx 0.5$, the error of this approximation is essentially negligible (less than 1% for RHex or Tailbot).

2) *Tailed Body Dynamics*: Defining for clarity the absolute tail angle, $\theta_t = \theta_b + \theta_r$, and using the balance of angular momentum about the COM of each body, the equations of motion for the full nonlinear tailed system are (see [40, Sec. IV])

$$\mathbf{M}(\theta_r) \begin{bmatrix} \ddot{\theta}_b \\ \ddot{\theta}_t \end{bmatrix} + \begin{bmatrix} m_r l_b l_t \sin \theta_r \dot{\theta}_t^2 \\ -m_r l_b l_t \sin \theta_r \dot{\theta}_b^2 \end{bmatrix} = \begin{bmatrix} 1 \\ -1 \end{bmatrix} \tau \quad (38)$$

with an inertia tensor

$$\begin{aligned} \mathbf{M}(\theta_r) &= \begin{bmatrix} I_b + m_r l_b^2 & -m_r l_b l_t \cos \theta_r \\ -m_r l_b l_t \cos \theta_r & I_t + m_r l_t^2 \end{bmatrix} \\ &= (I_b + m_r l_b^2) \frac{\xi_t}{1 - \xi_t} \begin{bmatrix} \frac{1 - \xi_t}{\xi_t} & -\eta \cos \theta_r \\ -\eta \cos \theta_r & 1 \end{bmatrix}. \end{aligned} \quad (39)$$

Inverting the inertia tensor yields an expression of the tailed body dynamics that, unlike the template (6), is both nonlinear and state dependent

$$\ddot{\theta}_b = \frac{\tau}{I_{d,t}(\theta_r)} - C_o(\theta_r, \dot{\theta}_b, \dot{\theta}_t) \quad (40)$$

where C_o is the Coriolis acceleration, and we define (by analogy to the template's driven inertia) the configuration-dependent inertia $I_{d,t}$

$$I_{d,t}(\theta_r) = \frac{(I_t + m_r l_t^2)(I_b + m_r l_b^2) - (m_r l_b l_t \cos \theta_r)^2}{I_t + m_r l_t^2 - m_r l_b l_t \cos \theta_r} \quad (41)$$

$$= (I_b + m_r l_b^2) \frac{1 - \frac{\eta^2 \xi_t}{1 - \xi_t} \cos^2 \theta_r}{1 - \eta \cos \theta_r}. \quad (42)$$

In general, the Coriolis terms are negligible for tailed systems with small η , and the anchoring can be accomplished with a constant (average) approximation of the driven inertia. In the simplest case of body-centered tails (i.e., $l_b = 0$, $\eta = 0$), $I_{d,t}$ reduces to I_b exactly and the Coriolis terms drop out, allowing the choice of $\Xi_{t,I_d}(\mathbf{p}_t) := I_b$.

Most of the tails considered in Table IV have $\xi_t \approx 0.5$, and therefore, for these tails, consider $I_{d,0.5} := I_{d,t}|_{\xi_t=0.5}$, which reduces exactly to

$$I_{d,0.5}(\theta_r) = (I_b + m_r l_b^2)(1 + \eta \cos \theta_r). \quad (43)$$

Integrating this function over a half tail sweep, $\theta_r \in [90^\circ \ 270^\circ]$ (approximating the range of motion of many tails in Table IV), yields the best approximation for these bodies

$$\bar{I}_{d,0.5}^* := (I_b + m_r l_b^2) \left(1 - \frac{2\eta}{\pi}\right). \quad (44)$$

In this paper, we choose this as our morphological reduction for the driven inertia, i.e., $\Xi_{t,I_d}(\mathbf{p}_t) := \bar{I}_{d,0.5}^*$, although other choices may work better for some systems. For each of the tailed systems surveyed in this paper, the average deviation from (42) is less than 15% over their actual tail range of motion; for RHex, the error is less than 2.5%.

3) *Final Error Due to Approximate Morphological Reduction*: Using the template relations to constrain the power required to meet the righting task is subject to error from three sources: variation in the connection vector field, the changing inertia tensor, and the Coriolis accelerations. This total error can be quantified over the tail design space (ξ_t, η) for a particular body/tail rotation task by applying the nondimensionalization [see (13)] to the nonlinear dynamics¹¹ and numerically integrating the resulting system (derived in [40, Sec. IV-A]), with the optimal values of no-load speed and switching time from the template, until the body comes to rest at a time \tilde{t}_n . Defining the final body error

$$e_b(\xi_t, \eta) := \tilde{\theta}(\tilde{t}_n) - 1 \quad (45)$$

and final time error

$$e_t(\xi_t, \eta) := \frac{\tilde{t}_n - \tilde{t}_f^*}{\tilde{t}_f^*} \quad (46)$$

which are plotted in Fig. 5(b) and (c) for a half sweep of the tail centered around $\theta_r = 180^\circ$. Final error for this maneuver is less than 10% across the large swath of parameter space containing the examples found in the literature thus far; in particular, time and angle error fall within 2% for RHex and within 4% for Tailbot.

B. Wheeled Morphological Reduction

A reaction wheel is a radially symmetric inertial appendage with mass centered at its joint and can be seen as a special case of a tail, with $l_t = 0$; the appendage is simply a rigid body with inertia I_w mounted a distance l_b from the body's COM (see Fig. 2). The parameter set for a reaction wheeled body is

$$\mathbf{p}_w := [m_b, I_b, l_b, m_w, I_w, s_r, P, \omega_m, t_s, \theta_{b,f}, t_f] \quad (47)$$

where, in general, the wheel stroke s_r is infinite.

The connection field (and, thus, equivalent tail effectiveness) follows from (36) as

$$\frac{\partial \theta_b}{\partial \theta_r} = -\frac{I_w}{I_w + I_b + m_r l_b^2} := -\xi_w. \quad (48)$$

Here, the vector field is a configuration-independent constant, as in the template, and therefore, the anchoring is exact. The dynamics are found simply by setting $l_t = 0$ in (38) and (39); the nonlinear terms disappear, and the dynamics become linear with driven inertia

$$I_{d,w} = I_b + m_r l_b^2. \quad (49)$$

The nonidentity components of the morphological reduction are, thus, chosen from (48) and (49), as listed in Table II.

¹¹This step isolates the effect of tail-specific geometry (ξ_t, η) from the remaining parameters so that error can be quantified with respect to tail parameters alone.

C. Limbed Morphological Reduction

Unlike the tail and reaction wheel anchors, whose kinematics' were more complex than the template's and consisted of a greater number of physical parameters but still represented a single DOF, an anchor model of a collection of limbs is truly a higher DOF mechanism. The general problem of finding "gaits" in this larger shape space that extremize body rotation has been explored in [41]; here, we consider the simpler cases that arise when the limbs are coordinated such that the effective shape space is 1-D. The resulting kinematics lie on a submanifold of the configuration space and, as we show, are equivalent to the kinematics of the simpler template model. Hence, the "anchoring" is accomplished through the active closed-loop control that coordinates the limbs.

In general, the effectiveness of an assemblage of limbs varies over their configuration space, even when coordinated. However, two interesting cases arise under certain conditions when all appendages are actively controlled to be parallel, that is, each leg's relative angle is commanded to be either $\theta_i = \theta_r$ or $\theta_i = \theta_r + 180^\circ$, for some common θ_r . Given N limbs arranged with pivots in a line coincident with the body's COM (typically the centerline of the robot's body), a sufficient condition¹² for configuration-independence of the connection field is that the limbs are identical (each with mass m_t , length l_t , and MOI I_t), and that the pivot locations are symmetric across the body COM (as with the limbs of RHex, for example). Let $m_{tot} := m_b + Nm_t$ represent the total system mass, and l_i the distance from body COM to the i th pivot location (generalizing the tail anchor's pivot offset l_b). The expression of the total angular momentum (derived in [40, Sec. V]) reduces considerably in two illuminating examples, depending on the phasing of the limbs (represented here by $s_i = \pm 1$, with s negative for legs out of phase with θ_r by 180°). The full parameter set for an N -limbed system with the symmetry condition above is

$$\mathbf{p}_\ell := [m_b, I_b, \ell_1, s_1, \dots, \ell_N, s_N, l_t, m_t, I_t, s_r, P, \omega_m, t_s, \theta_{b,f}, t_f]. \quad (50)$$

Here, we assume for simplicity that the limbs share the same range of motion s_r and the power P is taken to be the sum across all limbs.

RHex has six identical legs arranged in symmetric pairs of pivots along the centerline of the body, that is, $N = 6$, $l_1 = -l_3$, $l_2 = 0$, and all legs have equal mass m_t and length l_t . The pairs of legs are driven in antiphase to generate an alternating tripod gait when walking or running, a condition that could be modeled here by taking s_i negative for odd i and positive otherwise so that $\sum_{i=1}^6 s_i = 0$. In the antiphase case, the angular momentum reduces to

$$H_{O,l} = (I_p + N(I_t + m_t l_t^2))\dot{\theta}_b + N(I_t + m_t l_t^2)\dot{\theta}_r \quad (51)$$

where $I_p = I_b + m_t \sum_{i=1}^N \ell_i^2$. When all legs are in phase, $\sum_{i=1}^6 s_i = N$, and the angular momentum is

$$H_{O,l} = (I_p + N(I_t + m_{rt} l_t^2))\dot{\theta}_b + N(I_t + m_{rt} l_t^2)\dot{\theta}_r \quad (52)$$

¹²The necessary condition is considerably more general; see [40, Sec. V] for details.

TABLE III
COMPARISON OF PHYSICAL PROPERTIES FOR LIMBED OR WHEELED SYSTEMS WITH THE CAPABILITY FOR AERIAL REORIENTATION

Attribute	RHex	Cub	Hexbug	Dirt bike
Citation		[26]	[5]	[16]
Number in error figure	12	11	9	10
Appendage Type	Limbs	Limbs	Wheel	Wheel
Body length (cm), L	57	21	5	140
Body mass (g), m_b	7500	1300	40	105×10^3
App. mass (g), m_t	63	52	5	10×10^3
App. offset (cm), l_b, ℓ_i	25, 0, 25	10, 10	2.5	70
App. length (cm), l_t	10	6.3	0	0
Body inertia (kg-m ²), I_b	0.15	9.8×10^{-3}	17×10^{-6}	20
App. inertia (kg-m ²), I_t	0.46×10^{-3}	0.14×10^{-3}	12×10^{-6}	0.4
Effectiveness, ξ_ℓ, ξ_w	0.037	0.096	0.38	0.016
Driven inertia (kgm ²), I_d	0.17	0.012	19×10^{-6}	24
Peak motor power (W)	2052	23.3	0.34	33×10^3
Range of motion, s_r	360°	180°	360°	360°
App. speed (r/min), ω_m	434	77	916	1200

Unlike the tailed examples, these machines anchor without error.

with the subtle difference being the adjusted mass $m_{rt} := m_b m_t / m_{tot}$, a generalization of m_r . In either case, the connection field is constant and, thus, the equivalent template effectiveness is error-free

$$\Xi_{\ell,\xi}(\mathbf{p}_\ell) := \xi_\ell = \frac{N(I_t + m_k l_t^2)}{I_b + m_t \sum_{i=1}^N \ell_i^2 + N(I_t + m_k l_t^2)} \quad (53)$$

where $m_k = m_t$ when leg pairs are out of phase, and $m_k = m_{rt}$ when legs are in phase. Since $m_t > m_{rt}$, antiphase leg swings are more effective than in-phase swings, as explored further in Section IV-B.

The multibody dynamics of a robot with several phased appendages are considerably more complex than the developments of the previous sections and should be derived carefully for any particular case of interest. Here, we merely suggest a naïve mapping based on the rotating inertia, as expressed in the symmetric cases outlined in Section III-C

$$\Xi_{\ell,I_d}(\mathbf{p}_\ell) := I_{d,\ell} = I_b + m_t \sum_{i=1}^N \ell_i^2 \quad (54)$$

mapping the total input power across all limbs to the template.

IV. COMPARATIVE MORPHOLOGY AND SCALING

Each of the diverse IR bodies of the previous section can accomplish the given task, raising the question of how morphology shapes the available design choices. The differences can be expressed and compared directly through each system's morphological reduction, as summarized in Table II. In this section, we examine the consequences of those anchoring relations and explore the implications for IR at sizes large and small.

A. Examples From the Literature

To facilitate our comparative approach, we present examples of IR machines from the literature in Tables III and IV (compiled using the references shown and personal communications¹³). As

¹³Values differing from those in the cited references are more up-to-date or accurate.

TABLE IV
COMPARISON OF PHYSICAL PROPERTIES FOR TAILED SYSTEMS WITH THE CAPABILITY FOR AERIAL REORIENTATION

Attribute	RHex	Tailbot	TaYLROACH	2-DOF Tailbot	Jumper	Kangaroo	Jerboa	Cub
Citation		[2]	[4]	[32]	[3]	[9]	[25]	[26]
Number in error figure	1	2	3	4	5	6	7	8
Body length (cm), L	57	11.7	10	13.5	7.5	46	21	21
Body Mass (g), m_b	8100	160	46	105	25.1	5030	2270	1250
Tail Mass (g), m_t	600	17	4	70	1.4	371	150	310
Tail offset (cm), l_b	8	4.5	5	5.2	1	15.6	3	10
Tail length (cm), l_t	59	10.3	10.2	7.3	6.8	17.7	30	16.8
Body Inertia (kg-m ²), I_b	0.15	154×10^{-6}	39.6×10^{-6}	210×10^{-6}	9.3×10^{-6}	0.05	0.025	0.01
Tail Inertia (kg-m ²), I_t	0 ¹⁶	0 ¹⁶	0 ¹⁶	479×10^{-6}	6.4×10^{-6}	0.0172	0 ¹⁶	875×10^{-6}
Nonlinearity, η	0.136	0.437	0.49	0.227	0.072	0.339	0.1	0.529
Tail effectiveness, ξ_t	0.5587	0.4683	0.4396	0.6848	0.5705	0.3235	0.3351	0.3911
Peak Motor Power (W)	342	4	2.5	1.75	0.257	19	426	5.82
Driven inertia (kg-m ²), I_d	0.141	145×10^{-6}	37.2×10^{-6}	283×10^{-6}	9.02×10^{-6}	0.0482	0.0236	0.0092
Range of motion, s_r	172.5°	255°	265°	135°	280°	220°	180°	110°
Tail speed (r/min), ω_m	356	3000	400	320	1000	240	353	77
Error, final angle (45)	-1.29%	-1.90%	-1.26%	-4.78%	-0.630%	3.48%	1.48%	0.507%
Error, final time (46)	1.20%	3.92%	4.91%	0.105%	0.836%	5.75%	1.94%	6.59%

an interesting contrast with the mobile robots that are the focus of this paper, we included another notable example of terrestrial dynamic IR—a small off-road motorcycle (“dirt bike”), as skilled riders are known to modulate the acceleration of the rear wheel to control orientation during leaps and tricks [16]. Most use morphology designed especially for IR, but three machines (the two legged examples and the motorcycle) feature appendages designed for terrestrial locomotion that can be co-opted for aerial IR. The mass range covered by the examples is surprisingly large—over 300-fold among the tailed robots and over three orders of magnitude in all. This is not a comprehensive list of all robots harnessing inertial forces; notably, we have omitted devices where the tail moves in a plane far from the body COM, as in [7]. However, the diversity of the chosen machines provides both a verification of the efficacy of the templates-and-anchors design approach (noting the low final error for all machines) and enables some useful comparisons, as discussed in the following subsections.

B. Selection of Morphology for Inertial Reorientation

When is it appropriate to add a new appendage to a limbed body and when is it better to assign the inertial appendage role to a tail rather than a reaction wheel? In short, tails provide the most reasonable path to high values of effectiveness ($\xi \approx 0.5$ or higher) and are, thus, well suited to aggressive dynamic maneuvers, while reaction wheels provide infinite stroke over longer time scales. Limbs may provide a middle ground, varying considerably in morphology across extant robots, and thus in effectiveness, and may provide some IR capability without any additional payload.

1) *Wheeled Versus Tailed Bodies*: The symmetric mass of a reaction wheel provides the advantage of simple linear dynamics and infinite range of motion. Of course, large wheels become cumbersome more quickly than a tail—a practical reaction wheel could be no larger in diameter than a robot body’s smallest dimension. In natural systems, tails greater than body length are common and, thus, we can expect larger effectiveness from tails than from reaction wheels. For example, between the

comparably sized Hexbug [5] and TaYLROACH [4] (the former employing a pivot-centered double tail mass which acts like a wheel, and the latter an offset tail), the tailed design achieves roughly 15% higher effectiveness (0.44 versus 0.38) with 20% lower appendage mass (4g versus 5g; see Tables III and IV).

Since wheels and limbs need not incur the constrained range of motion suffered by practical 1-DOF tails,¹⁴ their effectiveness seems less important (i.e., it does not intrinsically limit body rotation)—so why bother with a relatively bulky tail? The answer is revealed through the power equation (22) and its inverse dependence on tail effectiveness. For a given task, a doubling of ξ reduces the power requirement by half. Herein lies the fundamental limitation of low-effectiveness devices for fast reorientation: a small flywheel will require much more power than a relatively long tail for the same maneuver. The short time scales available for aerial reorientation in terrestrial robots suggest a limited role for internal reaction wheels, but when this constraint is lifted (e.g., in space robotics [48]), such devices should be ideal. The motorcycle example in Table III provides an instructive exception—its IR “appendage” is driven by the machine’s locomotive powertrain, resulting in the largest body mass-specific power (over 300 W/kg) of any example here, enabling impressive aerial maneuverability in the right hands. When retrofitting an IR appendage to an existing machine, the lower power requirements of a tailed design should lead to generally lower added mass than a less effective wheel. For tails and wheels of comparable length scale, the advantage goes to the wheel due to the subtle effect of the reduced mass—the offset tail pulls the system COM toward the tail as appendage mass increases, thus decreasing effectiveness (m_r in ξ_t is strictly smaller than m_t).

2) *Limbed Versus Tailed Bodies*: For a given total added mass, a single appendage (tail) will generally provide larger effectiveness than two or more appendages. The squared dependence of effectiveness on length makes elongate appendages most attractive; hence, dividing a tail into two limbs each with

¹⁴More complex tails can escape this limitation in some maneuvers, e.g., the conical tail motion generating roll in the falling gecko [18].

half the length and mass of the original appendage would entail a significant loss of performance (a pair of symmetric flywheels sees a similar disadvantage). On the other hand, in many cases (for example RHex), limbs also provide infinite stroke, can exceed body dimensions without negative consequences (unlike a reaction wheel), and will by definition be already present on a legged terrestrial robot, eliminating any added cost or complexity. Machines with relatively long limbs will likely benefit most from this strategy (the quadruped Cheetah Cub achieves almost three times the IR effectiveness of RHex with a third fewer limbs; see Table III). However, the use of these appendages for aerial reorientation may pose significant drawbacks, most notably a constraint on their final orientation upon landing (touching down feet-first is typically desirable). The explicit design for reorientation will likely also conflict with other limb design priorities (for example, distal mass is typically a disadvantage when interacting impulsively with a substrate or when retracting the limb during the swing phase [49]). Still, in many cases, even a limb designed for running may result in enough inertial effectiveness to be useful in small (but significant) rotations. We will test this hypothesis in Section V-B.

3) *Core Versus Appendage Actuation*: A tailed body and an actuated spine [11], [47] can both be represented by the same anchor model, but represent very different design propositions. The primary advantage of a spine is that it may preserve the overall morphology (in particular volume and body envelope) by essentially separating the body into two chunks with much lower MOIs (with $\xi_t \approx 0.5$ if the segments are similar). Meanwhile, an added tail will, in general, extend the body envelope. The major drawback of body bending (as with using limbs for IR) is that the final orientation of both segments is important if the legs of the robot are to hit the ground simultaneously [47]—as we show in Section V-B, increasing the number of contact limbs when landing can greatly increase survivability. Furthermore, existing robotic platforms (like RHex) cannot be substantially altered without a major redesign, but their distal appendages may be relatively easy to add, subtract, or change. The core actuation approach may have increased advantages outside the planar scope of this paper; compare, for example, roll maneuvers in the falling cat [15] against those of the falling gecko [19].

4) *Maximizing Tail Performance*: Intuitively, tail effectiveness increases with tail mass, length, and inertia and decreases with the corresponding body parameters. Minimizing tail offset (placing the joint close to the body COM) has the dual benefits of increasing performance and reducing nonlinearity (the MSU jumping robot [3] comes closest to this ideal, while Tailbot could increase effectiveness by 10% by centering its tail at the body's COM). Concentrating tail mass at the appendage's extreme produces the most effectiveness per unit tail length (recall l_t is the distance from pivot to tail COM, which if $I_t \neq 0$ is strictly less than the total tail length) and, thus, an idealized tailed body consists of a point-mass tail pinned at the body's COM. Less intuitive is the tradeoff between tail mass and length; clearly, a given effectiveness can be accomplished with any number of combinations of each, although increasing tail mass eventually sees diminishing returns due to the effect of the reduced mass (31). By contrast, increasing tail length quadratically

increases effectiveness. RHex's relatively long tail achieves 75% higher effectiveness than that of the Kangaroo robot with approximately the same fraction of overall mass dedicated to appendage. At what point a tail's length becomes cumbersome is surely dependent on the constraints of other tasks and varies widely between applications, but the examples of Table III see tail lengths commonly exceeding one body length.

C. Scaling of Inertial Reorientation

Agile mobile robots span an increasingly large size range, raising the question of whether IR remains a practicable strategy for robots large and small. In the next section, we design a tail for RHex with a task specification based on the righting performance of Tailbot, a robot approximately 1/15 of RHex's mass. How will this mass difference dictate changes in morphology or mass-specific motor power? Because ξ is dimensionless and dependent only on morphology, isometrically [50] scaled robots are kinematically similar—for a given appendage rotation, the body rotation will be identical at any size scale. However, the power required for a maneuver will vary with size.

Consider a robot isometrically scaled by a length L . Assuming uniform density, the robot's mass will scale by L^3 and its inertia by L^5 . If the robot were required to reorient through the same angle in the same time regardless of size, then by substitution into (22) (replacing I_d with L^5 and dividing both sides of the inequality by L^3), we would require power per unit robot mass (power density of the whole machine) $P_d \propto L^2$. However, because gravity is constant, g , a larger robot will fall slower relative to its length (i.e., dynamic similarity [51]). For a free fall distance of $h \propto L$, the time available is $t_f = \sqrt{2h/g} \propto L^{1/2}$. Therefore, from (22), the required power per unit robot mass

$$P_d \propto \frac{I_d}{mt_f^3} \propto \frac{L^5}{L^3 L^{3/2}} = L^{1/2} \quad (55)$$

scales as the square root of length. This indicates that IR gets mildly more expensive at large size scales; larger robots may suffer reduced performance or must dedicate a growing portion of total body mass to tail actuation (or, noting the inverse relationship with ξ , to increased tail effectiveness). However, RHex and Tailbot span a characteristic length range of almost four-fold without dramatic differences in ability (see Fig. 7); in fact, the smaller machine dedicates more body mass to its tail motor than RHex (6.9% versus 3.3%), even as the larger machine has relatively higher body inertia (an isometrically scaled Tailbot of RHex's mass would have $I_b = 0.11 \text{ kg}\cdot\text{m}^2$, almost 30% lower than RHex). In this case, differences in actuator performance trump scaling—Tailbot uses a low-quality brushed motor, while RHex's higher quality components (see [11])—allow it to escape the penalty of size.

Intriguingly, generalization of the IR template dynamics suggests that (55) may govern scaling of other power-limited self-manipulation tasks, including aspects of legged locomotion. Consider a robot with its feet planted firmly on the ground, rotating its body in the yaw plane about an actuated hip. This situation could be modeled by a single rigid body, connected to the ground by a motor—that is, the system can be modeled by

the IR template, considering the ground to be the “appendage,” with I_a infinitely large and $\xi = 1$. Power for reorientation for this grounded reorientation task scales as in (55).¹⁵ In this simplified scenario, power-limited reorientation scales identically whether the body rotation is driven by inertial or ground reaction forces; we, therefore, hypothesize that inertial appendages may enhance agility at any size scale permitting legged maneuverability.

V. DESIGN FOR INERTIAL REORIENTATION

In this section, we present examples of the complementary design problems of body selection and performance evaluation (introduced in Section II) by exploring IR morphology for RHex. The first step in the body selection problem P1 is to specify the task or set of tasks required of the machine [i.e., parameterizing (1)]; the task and other (external) concerns will determine the overall morphology, subject to the tradeoffs discussed in the previous section. With a body plan chosen, the designer is then free to pick any set of physical parameters in \mathcal{R}_i that best meets performance needs outside the reorientation task. A naïvely rational design approach might introduce a cost function, $C(\mathbf{p}_i)$, expressing the impact of the IR morphology on some other critical task (e.g., legged locomotion) or penalty (e.g., parts cost) and solve the resulting constrained minimization task. However, it is notoriously difficult to encode robustness within the rigid optimization framework. Robots, putatively general-purpose machines, will typically be assigned multiple critical tasks, oft-times with conflicting objectives (e.g., fast locomotion and steady perception). More frequently, legacy constraints imposed by a robot’s existing design will further reduce the design problem to the selection of one or two parameters, precluding the possibility of an optimized design. Every design problem (whether of tails, limbs, flywheels, or other morphology) will likely entail its own set of constraints, assumptions, and objectives that must be chosen such that (28) results in a suitable and unique design solution.

In the performance evaluation problem P2, the fixed design restricts the system performance to a subset of task space (the projection of the feasible design set \mathcal{R} onto the $(\theta_{b,f}, t_f)$ subspace). This region can be computed for set values of ξ , I_d , P , s_r , and ω_m by using (12) to query the feasibility of a task (values of t_f and $\theta_{b,f}$), selecting the switching time t_s to satisfy the final angle condition, if possible. A fixed template design will necessarily be suboptimally geared for most tasks in the feasible task subspace; the cost of this suboptimality (along with that of submaximal current limit) can be calculated through the changing power cost k_p in (22). We compare the achievable task subspace for two implementations of IR morphology on RHex in Fig. 6 and list values of k_p where applicable.

In practice, the design process will use both the selection and evaluation problems to settle on a solution both practicable and task feasible. Starting with the body selection problem (parameterizing a task and choosing a body plan), the designer should

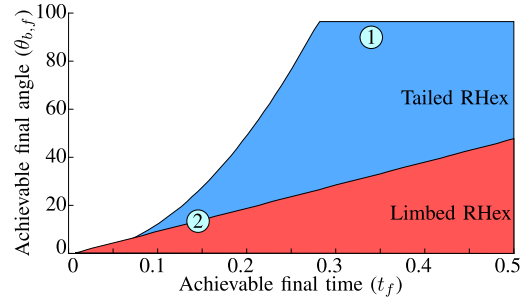


Fig. 6. Regions of task space (a projection onto the $\theta_{b,f}$ and t_f components of the feasible set \mathcal{R}) accessible by two instantiations of IR morphology on RHex for the reorientation task (1). The tail is limited by power for the quickest tasks and by stroke for slower maneuvers; its higher effectiveness allows for more useful rotation at relevant time scales. The numbers indicate the two experimentally validated tasks: 1) tailed reorientation in one body length fall and 2) limbed reorientation during a leap. Both tasks fall within the tailed body’s feasible set, but task 1 exceeds the limbed body’s capability.

first use \mathcal{R}_i^* to achieve a rough design, as the reduced (gearing-optimal) space and simpler form of the constraints will highlight the consequences of any choices (fixing legacy-constrained physical properties, or adding constraints to satisfy other task objectives). Since practical concerns will further limit parameter choices (e.g., the optimal powertrain is not likely to exist as an off-the-shelf product), the designer should then use performance evaluations of several candidate designs to find a feasible and physically realizable design. A major advantage of this approach over a straightforward optimization is that the effects of the inevitable deviations from optimality can be quantified and compared (e.g., through k_p), thus informing the designer’s concessions to practicability.

Real-world actuator selection is constrained by factors beyond rated power, as used in the preceding sections. Choosing a powertrain for a real system also involves characterizing motors by their electrical (current, voltage), thermal, legacy (constraints of the robot’s body), physical (size, mass), financial, and labor costs, as we show in the selection of the final motor for the following design experiments.

A. Appendage Design for RHex

1) *Tail Payload:* As an example of the body selection problem P1, we designed a tail for RHex by first specifying the task parameters and, then, using \mathcal{R}_i^* to guide the selection of the remaining values in \mathbf{p}_t ; the robot’s existing morphology further constrains our choices to a subset of \mathcal{R}_t .

In the interest of direct comparison with Tailbot [2], we selected task specifications based on replicating one element of the smaller robot’s behavioral repertoire: a reorientation of $\theta_{b,f} = 90^\circ$ in the course of falling one body length, L . For RHex, this translates to the task specification

$$\theta_{b,f} = 90^\circ, \quad t_f = \sqrt{\frac{2L}{g}} \approx 0.34 \text{ s} \quad (56)$$

where g is the gravitational acceleration. As discussed in Section IV-B, the large effectiveness easily achieved by a tail

¹⁵The scaling of relevant time scale (during a single step) again follows dynamic similarity, as stride frequency in running scales with \sqrt{L} [51].

makes that morphology the most attractive choice for this relatively aggressive maneuvering task [significantly decreasing the actuator requirements through the power equation (22)].

Of the full set of tailed-body parameters \mathbf{p}_t [see (29)], two (body mass and inertia) were already set by RHex's existing body morphology, and a third (pivot location) was constrained by the body's envelope. Confident that we could make the tail very nearly a point mass on a near massless rod (thus maximizing effectiveness per unit mass and length), we further eliminated I_t .¹⁶ While Tailbot was a special-built machine, the tail for RHex was added to the existing platform as a modular payload [11], and as such, the range of motion is significantly lower than Tailbot's. As the design of the modular payload system limits maximum tail sweep to 180° regardless of pivot position, we centered the tail along the body axis to minimize $l_b = 8$ cm [maximizing effectiveness, reducing η and further motivating the efficacy of (26)]; a small safety margin to avoid collision with the body reduced stroke slightly further to $s_r \leq 172.5^\circ$. With the selection of this range of motion limit, tail effectiveness is constrained by (26) to $\xi_t \geq 0.522$, leaving the question of the balance between tail length and mass. The addition of weight to RHex via external payload has known (small) performance costs, while the addition of a long tail has unpredictable and potentially large consequences on capability outside of aerial righting; we, therefore, chose to minimize tail length by selecting an additional mass constraint based on previous experiences with modular payloads, $m_t \leq 0.6$ kg (giving $m_r = 0.56$ kg). With $I_t \approx 0$, the minimum tail length to meet the effectiveness requirement can be found directly from the definition of ξ_t (see Table II) and is $l_t \geq 0.55$ m. As assembled, RHex's actual tail effectiveness is slightly larger than required and is about 20% larger than that of Tailbot (see Table IV), as needed to achieve feasibility respecting the stroke constraint consequent upon the roughly 30% reduction of its tail stroke relative to that of the smaller machine.

Meeting the body stroke specification fixed all parameters save motor power, which is constrained by the second inequality in (26); the smallest allowable value of P satisfying this constraint is approximately 39 W, with an optimal no-load speed just over 2 Hz. The Maxon pancake motors that drive RHex's legs are rated for 50-W continuous operation and can achieve transient output up to 342 W [11], but practical concerns including thermal safety limit current to 12 A, just 33% of transient stall current (see Appendix C). A putative design using these motors falls well within \mathcal{R}_t despite their suboptimal gearing of 28:1 (effective $\tilde{\omega}_m \approx 1.0$, $\beta = 0.33$ giving $k_{p,t} \approx 11$ for this task, roughly four times higher than optimal); we found that mitigation of integration issues outweighed any possible weight savings that could be had by choosing a smaller motor with more optimal gearing. The chosen design is capable of rotating the body to 90° within a predicted final time of approximately 300 ms, well within the performance specification. This tailed design is tested in Section V-B1.

¹⁶The mass-centered rotational inertia of a small mass on a light rod is far smaller than the offset inertia, $m_r l_t^2$; the I_t value of this tail was, therefore, reported as zero in the cited work.

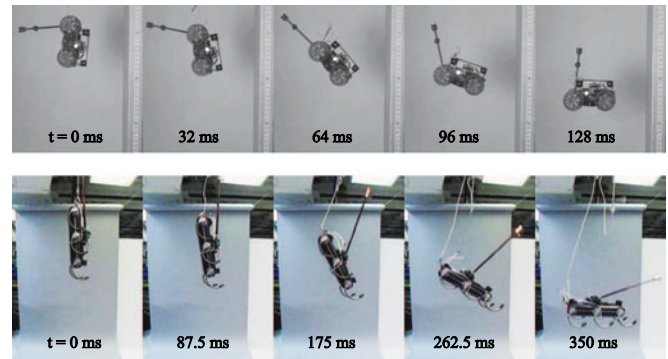


Fig. 7. Dynamically similar aerial righting in two robots spanning a 60-fold mass range: Tailbot (top) and RHex (bottom). Each machine rotates 90° in approximately one body length of fall.

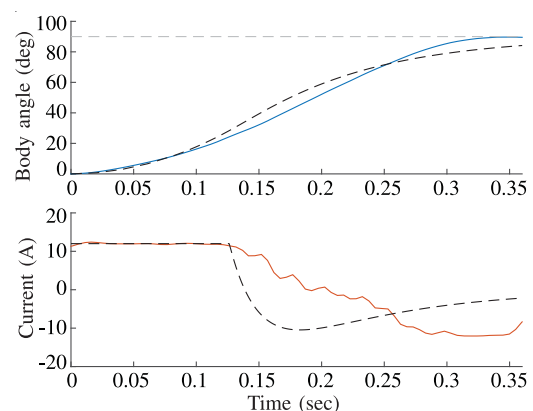


Fig. 8. Logged data from a tailed robot experiment. (Top) Body angle, from high-speed video (blue) and predicted by template with PD controller (dashed); (bottom) motor current, applied (red) and predicted by template (dashed). Disagreement between model and template is primarily due to unmodeled compliance in the tail pivot and shaft.

2) *Flailing Limbs*: A highly attractive alternative to the added complexity of a tail is to simply use RHex's existing limbs, preferably in the in-phase condition so as to land on all six simultaneously. The total reorientation effectiveness, as predicted by (53), is $\xi_\ell = 0.037$ (see Table III). With \mathbf{p}_ℓ fixed by the existing design, we can query (12) to check the feasibility of this body with respect to the task, (56). The unlimited limb rotation means the design trivially meets the stroke specification, but not within the final time (see Fig. 6). The very low effectiveness of the combined limbs necessitates almost eight full swings of the limbs to complete the body stroke requirement of (56) and, thus, a substantially different power train than is used for terrestrial locomotion: the optimal no-load speed for the limbed design of 2178 r/min is almost 13 times higher than RHex's maximum leg speed.

While RHex's existing morphology is inadequate for this highly agile task, its limbs still provide a potentially useful IR capability—the limbed system can rotate 32.3° in one body length of fall, or over 50° in the 1.36-m fall we used to test RHex's tail (see Fig. 6). Such small reorientations could be significant especially when running, where the nominal body



Fig. 9. RHex surviving a run off a cliff outdoors.

orientation varies a similarly small amount [52]. One full rotation of RHex's six limbs produces 13.3° of body rotation, and its powertrain can achieve this reorientation in as little as 150 ms. This new reorientation task fits easily into the aerial phase of a single leap, usefully allowing modulation of landing angle; we test it empirically in Section V-B2.

B. Experiments on RHex

1) *Inertial Reorientation Task Implemented on the Tailed-Body RHex Design:* As an anecdotal validation of the foregoing scaling arguments, we conducted a series of IR experiments on RHex (see Figs. 7 and 8). In the first experiment, the robot was dropped nose first from a height of 1.36 m [over eight times the standing height and 2.7 times the body length, although we still required the robot to meet the task specification in (56)].

We implemented a PD controller on the internal angle in lieu of a bang–bang controller—as discussed in Appendix B, the saturated PD controller converges to the bang–bang design given large enough gains. In practice, the sensor bandwidth and other unmodeled effects result in oscillation around the regulated angle; therefore, we relaxed the high-gain requirement slightly, accepting the slight performance cost in favor of the extra robustness provided by the closed-loop design (the effective current switching time of approximately 0.22 s corresponds to a $\tilde{t}_s \approx 2.85$, slightly later than the optimal 2.40 for the chosen gearing and current limit). The legs were simultaneously controlled to point toward the ground.

Data from a typical reorientation experiment can be seen in Fig. 8; we logged sensor data and shot high-speed video at 210 frames/s. The robot rotated to within 1° of horizontal before landing on all six legs, taking about 350 ms to complete the reorientation, corresponding to a dimensionless halting time of approximately 4.55, and a corresponding power cost $k_p \approx 23.5$ —more than nine times optimal and twice the cost predicted in Section V-A1, due to the suboptimal controller and several unmodeled effects. Drivetrain losses decreased output torque by roughly 25% and the tail mount and carbon fiber shaft exhibited substantial elasticity, causing acceleration lag and increasing the deviation from bang–bang torque application. Despite the high cost of the suboptimal design, the robot completes the task within 3% of the target time. As further verification of the template, we added the PD controller and drivetrain efficiency losses to the model; simulation of this more accurate (suboptimal) template is plotted against experimental data in Fig. 8.

When dropped with the tail controller off, the robot impacted the ground nose first, with only the front pair of legs in support. The impacted limbs quickly snapped, allowing the robot's body

to strike the ground, causing internal damage. We, therefore, conclude that the active inertial tail substantially expands the task space of RHex by tripling the number of support limbs available for impact mitigation (thereby roughly tripling the strain energy tolerable before failure and increasing the survivable falling height).

To demonstrate this new ability for RHex in a practical task, the robot was also tested outdoors running along and then off of a 62-cm (3.8 hip heights or 1.2 body lengths) cliff. This stabilization task is governed by a different set of performance constraints that could be probed analogously to our approach to the reorientation task in Section II-C1¹⁷; in lieu of a more exhaustive analytic exploration of this task space, we note that this fall nearly saturated RHex's tail stroke and likely represents a near-limit for full stabilization at this running speed. The robot's inertial sensors detect the cliff upon initial body pitch and then actuate the tail according to the same PD control policy, landing the robot on its feet (see Fig. 9). As with the indoor experiments, a test with RHex running off a cliff with a passive tail confirmed that the robot lands nose first.

2) *Inertial Reorientation Template Anchored on RHex as a Limbed Body:* Finally, a third set of experiments tested the ability of RHex's legs to work as inertial tails. The existing limb design is incapable of achieving the original task (90° body rotation in 0.34 s; see Fig. 6), and so instead a feasible task consisting of a single rotation is used instead to test the flail kinematics. As first reported in [33, Sec. IV-C.5], after leaping vertically into the air, all of the legs were recirculated together to the same landing angle. Using the legs in phase for this experiment allows the robot to land on all six, although using the legs out of phase would have increased the effectiveness by about 3.5% (see Section III-C).¹⁸ The limbs were rotated clockwise in the first experiment and counterclockwise in the second for a net difference of 360° in stroke; the difference in final body angle between the two cases was 14° . While the leap gave only enough time for a single revolution of the limbs, the resulting body rotation made an appreciable difference in the quality of the landing, supporting our hypothesis that IR with even unspecialized limbs can be useful.

¹⁷The stabilization task could be specified by keeping the body angle within some allowable deviation over a time horizon t_f by swinging the tail to mitigate an impulse characterized by \dot{H} as in (4). Constraints analogous to (26) could be derived by solving the template kinematics and dynamics subject to this new task.

¹⁸As in the tailed trials, we used a PD controller on the internal angle (see Appendix B); however, here, this single control effort was pulled back into the more complicated limbed body through an anchoring controller (specifically, six independent PD controllers each regulating a limb to the common commanded position).

VI. CONCLUSION

As mobile robots proliferate in the complexity of both their morphology and behavioral scope, there is a growing need for principled methodology relating their body design to their capability. The templates-and-anchors approach adopted for this paper provides a unifying framework for the comparative morphology of robots (and even animals) and a practical approach to the design and evaluation of IR performance on real robots. We defined the IR template, the simplest model of an IR maneuver, equipped with a DC-motor-like model parameterized by peak output power. The template revealed the particular importance of a single parameter, defined here as IR effectiveness, which prescribed both the appendage rotation needed to move a body and the power needed to do so in fixed time. Dimensional analysis of template behavior revealed that a relatively modest increase in power density (growing with the square root of length) should be required to retain righting performance as platform size increases.

The model’s linear dynamics, along with a bang–bang controller, enabled analytic solution of the template’s single-switch reorientation behavior, revealing a simple relationship between morphology and performance, described by the task-feasible set \mathcal{R} [see (12)]. We then showed how the feasible set could be “pulled back” through a more complex body’s morphological reduction (defined as the possibly approximate mapping between parameter spaces of real robot body and abstracted template) to provide design restriction to a more usefully diverse set of machines. The resulting set of feasible real designs (28) retains enough freedom (e.g., allowing length to trade for mass) to afford some “optimization” in the sense of minimizing the impact of the design on other task abilities. In practice, concessions to practicality will necessitate deviations from optimality; fortunately, our framework gives the designer flexibility to compare candidate (suboptimal) designs and even quantify the performance cost of those compromises [e.g., through (23)].

Our approach facilitated the design of a tail for RHex, enabling IR capabilities dynamically similar to the much smaller Tailbot. A separate anchoring to the same template quantified the capability of RHex’s existing appendages (its six semicircular legs) to produce useful reorientation in their own right and revealed a preferred posture for doing so. A recent proliferation of tails (and other high-effectiveness appendages) for inertial righting allows us to calculate and compare effectiveness across a number of independent designs; generally, their effectiveness is close to 0.5, where the connection becomes configuration independent. As a result, these designs anchor nicely to the IR template with relatively low error. We expect that most well-designed appendages will fall within this paradigm.

The constraints making up \mathcal{R} and its gearing-optimal refinement (26) revealed general principles of design for righting morphology, while the morphological reductions provided crucial insight into the tradeoffs of each body type; we provide a detailed discussion in Section IV. Tails are a natural choice for fast large-amplitude IR, owing to the ease at which they can be designed for high effectiveness values without disrupting the existing platform morphology. However, as legged robots

increase the numbers of DOFs in limbs and body alike, these affordances should provide compelling sources of IR as well. In practice, the choice of anchor morphology for enabling IR in a robot is tightly coupled to overall function with respect to its mission, historical and other constraints on body design, and the task-specific rewards for high reorientation performance.

While the present analysis focuses on purely aerial maneuverers, inertial appendages also show promise in a variety of terrestrial tasks, stabilizing or actuating turns [4], [6], or stabilizing pitch over obstacles [2]. Likewise, inertial appendages have utility beyond the sagittal plane for aerial maneuverers, with out-of-plane appendage swings capable of effecting body rotations in yaw and roll as well as pitch, e.g., [19] and [32]. We postulate that tail effectiveness will remain a useful metric in these arenas as well, although the analysis of the dynamics and control affordance underpinning such behaviors remains an open problem.

APPENDIX A

GENERALIZED TEMPLATE–ANCHOR RELATIONSHIP

This section develops a general framework for the anchoring of more complex dynamical systems to a simpler template dynamical system [37]. This is a more general notion of anchoring than in, e.g., [53], which requires the template dynamics be, “conjugate to the restriction dynamics of the anchor on an attracting invariant submanifold,” or in [10, Sec. 1.2], which seeks, “controllers whose closed loops result in a low-dimensional attracting invariant submanifold on which the restriction dynamics is a copy of the template.”

In particular, consider two dynamical systems: the “template” X and the “anchor” Y . Each system has a state ($x \in \mathcal{X}$ and $y \in \mathcal{Y}$, respectively), control input ($u_X \in \mathcal{U}_X$ and $u_Y \in \mathcal{U}_Y$, respectively), parameter set ($p_X \in \mathcal{P}_X$ and $p_Y \in \mathcal{P}_Y$, respectively), and dynamics ($\dot{x} = f_X(x, u_X, p_X)$ and $\dot{y} = f_Y(y, u_Y, p_Y)$, respectively). The template is the simpler model; therefore, in general, $\dim \mathcal{X} \leq \dim \mathcal{Y}$.

The generalized anchoring is a specification of a set of mappings between the state spaces, control inputs, and parameter sets of the template and anchor. Specifically, define a state reduction, $h : \mathcal{Y} \rightarrow \mathcal{X}$, that anchors the state space, and its right-inverse, $h^\dagger : \mathcal{X} \rightarrow \mathcal{Y}$, such that $h \circ h^\dagger = id_{\mathcal{X}}$. Let Dh and Dh^\dagger be the Jacobians of these maps. Define similarly a control reduction,¹⁹ $g : \mathcal{U}_Y \rightarrow \mathcal{U}_X$, that anchors the control input, and its right-inverse, $g^\dagger : \mathcal{U}_X \rightarrow \mathcal{U}_Y$, such that $g \circ g^\dagger = id_{\mathcal{U}_X}$. Finally, define a parameter or morphological reduction, $\Xi : \mathcal{P}_Y \rightarrow \mathcal{P}_X$, that anchors the parameter space, and its right-inverse, $\Xi^\dagger : \mathcal{P}_X \rightarrow \mathcal{P}_Y$, such that $\Xi \circ \Xi^\dagger = id_{\mathcal{P}_X}$. Collectively these six maps fully define the anchoring of Y in X .

An anchoring will be called exact if

$$f_Y(y, u_Y, p_Y) = Dh^\dagger \circ f_X(h(y), g(u_Y), \Xi(p_Y)) \quad (57)$$

¹⁹Note that often the control input will be a subset of the cotangent bundle over the state space, $\mathcal{U}_X \subset T^*\mathcal{X}$ and $\mathcal{U}_Y \subset T^*\mathcal{Y}$, i.e., force or torque applied to one or more coordinates. In this case, the control embedding may be related to the state space embedding, $g := \pi_{U,Y}(Dh^\dagger)^T$, i.e., the projection down to the appropriate coordinates of the transpose of the Jacobian of h^\dagger .

which implies that

$$f_X(x, u_X, p_X) = Dh \circ f_Y(h^\dagger(x), g^\dagger(u_X), \Xi^\dagger(p_X)) \quad (58)$$

(although the reverse is not necessarily true). By contrast, an anchoring will be called approximate if this relationship is only approximately true (up to some desired tolerance).

Define a template controller, $\tau_X : \mathcal{X} \times \mathcal{P}_X \rightarrow \mathcal{U}_X$, which may be applied by assigning $u_X = \tau_X(x, p_X)$. Similarly, define an anchor controller, $\tau_Y : \mathcal{Y} \times \mathcal{P}_Y \rightarrow \mathcal{U}_Y$, which may be applied by assigning $u_Y = \tau_Y(y, p_Y)$. The template controller may be pulled back into the anchor via the choice

$$\tau_Y(y, p_Y) := g^\dagger \circ \tau_X(h(y), \Xi(p_Y)). \quad (59)$$

An anchoring will be called passive if this is the only control authority exerted on the anchor system. By contrast, an anchoring will be called active if there is an additional anchoring controller, $\bar{\tau}_Y$, exerted in order to achieve the exact or approximate anchoring, i.e.,

$$u_Y = \tau_Y(y, p_Y) + \bar{\tau}_Y(y, p_Y) \quad (60)$$

where $\bar{\tau}_Y$ lies in the null space of g .

In this paper, we consider three anchor systems: one that has a passive exact anchoring, one that has a passive approximate anchoring, and one that has an active exact anchoring. For the passive anchors, $\mathcal{X} = \mathcal{Y}$ and $\mathcal{U}_X = \mathcal{U}_Y$ —therefore, the maps h , h^\dagger , g , and g^\dagger are all identity. The active anchor, through the additional controller $\bar{\tau}_Y$, restricts down to the template dynamics exactly, and so, these maps are similarly uninteresting. Therefore, this paper's focus is on the remaining anchoring functions Ξ and Ξ^\dagger and on the design of the template parameters and controllers to achieve the task.

APPENDIX B

ALTERNATE TEMPLATE CONTROLLER FORMULATIONS

For additional robustness, the template controller may use PD feedback on the body angle (relative to the desired final position, $\theta_{b,f}$, and velocity, $\dot{\theta}_b = 0$). The controller torque takes the form

$$\tau = K_p(\theta_{b,f} - \theta_b) + K_d(0 - \dot{\theta}_b) \quad (61)$$

subject to the limits imposed by the motor model. Given high enough gains, the torque will saturate, producing speed-limited acceleration and current-limited braking as in the switched case; the effective switching time (when $\tau = 0$) depends on the ratio of controller gains.

The ratio of gains that produces the optimal switch is found by examining the point where the acceleration switches signs, i.e., when the terms of (61) are equal; plugging in the angle and velocity at the time of switch and applying the spatiotemporal transformation (13) yields the ratio for the optimal value of $\tilde{\mathbf{p}}$ (see [40, Sec. II-B] for this derivation). After scaling back to physical torques, the optimally switching gain ratio is

$$\frac{K_d}{K_p} \approx \frac{0.26}{\gamma}. \quad (62)$$

Servoing on the internal angle produces an equivalent formulation for the PD controller. In the dimensioned zero angular

momentum template with initial conditions $\theta_b = \dot{\theta}_b = 0$, the connection field [see (5)] can be integrated to yield $\theta_b = -\xi\theta_r$. Starting with a PD controller servoing the body angle to a desired orientation $\theta_{b,d}$

$$\begin{aligned} \tau &= K_p(\theta_{b,d} - \theta_b) + K_d(0 - \dot{\theta}_b) \\ &= -K'_p(\theta_{r,d} - \theta_r) - K'_d(0 - \dot{\theta}_r) \end{aligned} \quad (63)$$

where $K'_p := \xi K_p$, $K'_d := \xi K_d$, and the desired appendage angle $\theta_{r,d} := -\theta_{b,d}/\xi$. The control torque on the appendage is opposite in sign to the body angle controller, as expected.

APPENDIX C

DIMENSIONLESS CONSTRAINTS FOR CURRENT-LIMITED DYNAMICS

If the maximum allowable torque (equivalently motor current) is limited to some factor $\beta \in (0, 1)$ less than the stall torque of the motor $\tau_\ell = \beta\tau_m$, the optimal reorientation consists of three phases: a constant torque phase until the acceleration becomes voltage limited, then a phase following the speed–torque curve of the motor until the controlled switch at \tilde{t}_s , followed by a constant braking torque phase until \tilde{t}_h . These dynamics can be integrated to produce a current-limited equivalent to \mathcal{R} . Alternatively, equivalent functions to \tilde{g}_h and \tilde{g}_θ can be used to calculate k_p , k_s , and k_t given β and a parameter set \mathbf{p} . We provide those equivalent relations here; their full derivations can be found in [40, Sec. I-A]

$$\tilde{g}_h(\tilde{\omega}_m, \tilde{t}_s, \beta) := \tilde{t}_s + \frac{\tilde{\omega}_m^2}{\beta} \left(1 - \beta \exp\left(\frac{-(\tilde{t}_s - \tilde{t}_\ell)}{\tilde{\omega}_m^2}\right) \right) \quad (64)$$

$$\begin{aligned} \tilde{g}_\theta(\tilde{\omega}_m, \tilde{t}_s, \beta) &:= \tilde{\omega}_m \tilde{t}_s + \tilde{\omega}_m^3 (\beta - 1) \exp\left(\frac{1 - \beta}{\beta} - \frac{\tilde{t}_s}{\tilde{\omega}_m^2}\right) \\ &\quad + \frac{\beta \tilde{\omega}_m^3}{2} \left(1 - \exp\left(\frac{2(1 - \beta)}{\beta} - \frac{2\tilde{t}_s}{\tilde{\omega}_m^2}\right) \right). \end{aligned} \quad (65)$$

ACKNOWLEDGMENT

Some of the data in Tables III and IV was collected through personal communication with the authors of the cited work. The authors would like to thank N. Kohut, J. Zhao, P.-C. Lin, A. De, and S. Heim for contributing to these morphometric data. The motorcycle example used information from Zero Motorcycles, Zero FX. The authors would also like to thank P. Nidamaluri for building the X-RHex tail, A. Effron and the four anonymous reviewers for their notes on the manuscript, and D. Hallac, J. Starr, A. De, R. Knopf, M. Choi, J. Coto, and A. Farabaugh for help with RHex and experiments.

REFERENCES

- [1] A. M. Johnson *et al.*, "Tail assisted dynamic self righting," in *Proc. Int. Conf. Climbing Walking Robots*, Baltimore, MD, USA, Jul. 2012, pp. 611–620.
- [2] E. Chang-Siu, T. Libby, M. Tomizuka, and R. J. Full, "A lizard-inspired active tail enables rapid maneuvers and dynamic stabilization in a terrestrial robot," presented at *IEEE/RSJ Int. Conf. Intell. Robots Syst.*, San Francisco, CA, USA, Sep. 2011.

- [3] J. Zhao *et al.*, “MSU Tailbot: Controlling aerial maneuver of a miniature-tailed jumping robot,” *IEEE/ASME Trans. Mechatronics*, vol. 20, no. 6, pp. 2903–2914, Dec. 2015.
- [4] N. Kohut *et al.*, “Precise dynamic turning of a 10 cm legged robot on a low friction surface using a tail,” in *Proc. IEEE Int. Conf. Robot. Autom.*, 2013, pp. 3299–3306.
- [5] C. Casarez, I. Penskiy, and S. Bergbreiter, “Using an inertial tail for rapid turns on a miniature legged robot,” in *Proc. IEEE Int. Conf. Robot. Autom.*, 2013, pp. 5469–5474.
- [6] A. Patel and M. Braae, “Rapid turning at high-speed: Inspirations from the cheetah’s tail,” in *Proc. IEEE/RSJ Int. Conf. Intell. Robots Syst.*, 2013, pp. 5506–5511.
- [7] R. Briggs, J. Lee, M. Haberland, and S. Kim, “Tails in biomimetic design: Analysis, simulation, and experiment,” in *Proc. IEEE/RSJ Int. Conf. Intell. Robots Syst.*, 2012, pp. 1473–1480.
- [8] J. Ackerman and J. Seipel, “Energy efficiency of legged robot locomotion with elastically suspended loads,” *IEEE Trans. Robot.*, vol. 29, no. 2, pp. 321–330, Apr. 2013.
- [9] G.-H. Liu *et al.*, “A bio-inspired hopping kangaroo robot with an active tail,” *J. Bionic Eng.*, vol. 11, no. 4, pp. 541–555, 2014.
- [10] R. Altendorfer *et al.*, “RHex: A biologically inspired hexapod runner,” *Auton. Robots*, vol. 11, no. 3, pp. 207–213, 2001.
- [11] G. C. Haynes *et al.*, “Laboratory on legs: An architecture for adjustable morphology with legged robots,” *Proc. SPIE*, vol. 8387, no. 1, p. 83870W, 2012.
- [12] M. Pijnappels *et al.*, “Armed against falls: The contribution of arm movements to balance recovery after tripping,” *Exp. Brain Res.*, vol. 201, no. 4, pp. 689–699, 2010.
- [13] L. S. Crawford and S. S. Sastry, “Biological motor control approaches for a planar diver,” in *Proc. IEEE Conf. Decision Control*, 1995, vol. 4, pp. 3881–3886.
- [14] T. Hedrick, J. Usherwood, and A. Biewener, “Low speed maneuvering flight of the rose-breasted cockatoo (*Eolophus roseicapillus*). II. Inertial and aerodynamic reorientation,” *J. Exp. Biol.*, vol. 210, no. 11, pp. 1912–1924, 2007.
- [15] T. Kane and M. Scher, “A dynamical explanation of the falling cat phenomenon,” *Int. J. Solids Struct.*, vol. 5, no. 7, pp. 663–666, 1969.
- [16] M. Brearley, “Motor cycle long jump,” *Math. Gazette*, vol. 65, no. 433, pp. 167–171, 1981.
- [17] T. Libby *et al.*, “Tail-assisted pitch control in lizards, robots and dinosaurs,” *Nature*, vol. 481, no. 7380, pp. 181–184, 2012.
- [18] A. Jusufi, D. I. Goldman, S. Revzen, and R. J. Full, “Active tails enhance arboreal acrobatics in geckos,” *Proc. Nat. Acad. Sci.*, vol. 105, no. 11, pp. 4215–4219, 2008.
- [19] A. Jusufi, D. T. Kawano, T. Libby, and R. J. Full, “Righting and turning in mid-air using appendage inertia: Reptile tails, analytical models and bio-inspired robots,” *Bioinspir. Biom.*, vol. 5, no. 4, p. 045001, 2010.
- [20] G. J. Zeglin, “Uniroo—A one legged dynamic hopping robot,” B.S. thesis, Massachusetts Inst. Technol., Cambridge, MA, USA, 1991.
- [21] K. Autumn *et al.*, “Robotics in scansorial environments,” in *Proc. SPIE Defense Security*, 2005, pp. 291–302.
- [22] S. Kim, A. T. Asbeck, M. R. Cutkosky, and W. R. Provancher, “SpinybotII: climbing hard walls with compliant microspines,” in *Proc. IEEE Int. Conf. Adv. Robot.*, 2005, pp. 601–606.
- [23] R. Balasubramanian, A. Rizzi, and M. T. Mason, “Legless locomotion: A novel locomotion technique for legged robots,” *Int. J. Robot. Res.*, vol. 27, no. 5, pp. 575–594, May 2008.
- [24] A. Demir *et al.*, “Inertial redirection of thrust forces for flight stabilization,” presented at *Int. Conf. Climbing Walking Robots*, Baltimore, MD, USA, Jul. 2012.
- [25] A. De and D. E. Koditschek, “The Penn Jerboa: A platform for exploring parallel composition of templates,” arXiv:1502.05347, Feb. 2015.
- [26] S. W. Heim *et al.*, “On designing an active tail for body-pitch control in legged robots via decoupling of control objectives,” presented at *Int. Conf. Climbing Walking Robots*, Hangzhou, China, Sep. 2015.
- [27] A. Crespi, K. Karakasiliotis, A. Guignard, and A. J. Ijspeert, “Salamandra robotica II: An amphibious robot to study salamander-like swimming and walking gaits,” *IEEE Trans. Robot.*, vol. 29, no. 2, pp. 308–320, Apr. 2013.
- [28] M. Estrada, E. W. Hawkes, D. L. Christensen, and M. R. Cutkosky, “Perching and vertical climbing: Design of a multimodal robot,” in *Proc. IEEE Int. Conf. Robot. Autom.*, 2014, pp. 4215–4221.
- [29] C. Kessens and C. T. Lennon, “Robotic uses of tails: Self-righting,” presented at *Robot.: Sci. Syst. Workshop “Robot. Uses Tails,”* Rome, Italy, Jul. 2015.
- [30] A. Jusufi, Y. Zeng, R. J. Full, and R. Dudley, “Aerial righting reflexes in flightless animals,” *Integrative Comparative Biol.*, vol. 51, no. 6, pp. 937–943, 2011.
- [31] A. Patel and E. Boje, “On the conical motion and aerodynamics of the cheetah tail,” presented at *Robot.: Sci. Syst. Workshop “Robot. Uses Tails,”* Rome, Italy, Jul. 2015.
- [32] E. Chang-Siu *et al.*, “A nonlinear feedback controller for aerial self-righting by a tailed robot,” in *Proc. IEEE Int. Conf. Robot. Autom.*, May 2013, pp. 32–39.
- [33] A. M. Johnson and D. E. Koditschek, “Legged self-manipulation,” *IEEE Access*, vol. 1, pp. 310–334, 2013.
- [34] J. P. Dyhr *et al.*, “Autostabilizing airframe articulation: Animal inspired air vehicle control,” in *Proc. IEEE Conf. Decision Control*, 2012, pp. 3715–3720.
- [35] M. M. Porter *et al.*, “Why the seahorse tail is square,” *Science*, vol. 349, no. 6243, 2015.
- [36] B. Grossi *et al.*, “Walking like dinosaurs: Chickens with artificial tails provide clues about non-avian theropod locomotion,” *PloS One*, vol. 9, no. 2, p. e88458, 2014.
- [37] R. Full and D. Koditschek, “Templates and anchors: Neuromechanical hypotheses of legged locomotion on land,” *J. Exp. Biol.*, vol. 202, no. 23, pp. 3325–3332, 1999.
- [38] A. Rizzi and D. Koditschek, *Further Progress in Robot Juggling: Solvable Mirror Laws*. Washington, DC, USA: IEEE Comput. Soc. Press, 1994, pp. 2935–2940.
- [39] J. Nakanishi, T. Fukuda, and D. E. Koditschek, “A brachiating robot controller,” *IEEE Trans. Robot. Autom.*, vol. 16, no. 2, pp. 109–123, Apr. 2000.
- [40] T. Libby *et al.*, “Technical report on: Comparative design, scaling, and control of appendages for inertial reorientation,” Univ. Pennsylvania, Philadelphia, PA, USA, *Tech. Rep.*, 2015. [Online]. Available: <http://kodlab.seas.upenn.edu/Aaron/TailsTR>
- [41] R. L. Hatton and H. Choset, “Geometric motion planning: The local connection, Stokes’ theorem, and the importance of coordinate choice,” *Int. J. Robot. Res.*, vol. 30, no. 8, pp. 988–1014, 2011.
- [42] P. Gregorio, M. Ahmadi, and M. Buehler, “Design, control, and energetics of an electrically actuated legged robot,” *IEEE Trans. Syst., Man, Cybern. B, Cybern.*, vol. 27, no. 4, pp. 626–634, Aug. 1997.
- [43] B. Hannaford and J. Winters, “Actuator properties and movement control: biological and technological models,” in *Multiple Muscle Systems*. New York, NY, USA: Springer, 1990, pp. 101–120.
- [44] J. E. Bobrow, S. Dubowsky, and J. Gibson, “Time-optimal control of robotic manipulators along specified paths,” *Int. J. Robot. Res.*, vol. 4, no. 3, pp. 3–17, 1985.
- [45] M. Tarkiaainen and Z. Shiller, “Time optimal motions of manipulators with actuator dynamics,” in *Proc. IEEE Int. Conf. Robot. Autom.*, 1993, pp. 725–730.
- [46] V. G. Rao and D. S. Bernstein, “Naive control of the double integrator,” *IEEE Control Syst.*, vol. 21, no. 5, pp. 86–97, Oct. 2001.
- [47] T. W. Mather and M. Yim, “Modular configuration design for a controlled fall,” presented at *IEEE/RSJ Int. Conf. Intell. Robots Syst.*, St. Louis, MO, USA, Oct. 2009.
- [48] Y. Umetani and K. Yoshida, “Resolved motion rate control of space manipulators with generalized Jacobian matrix,” *IEEE Trans. Robot. Autom.*, vol. 5, no. 3, pp. 303–314, Jun. 1989.
- [49] S. Seok *et al.*, “Design principles for highly efficient quadrupeds and implementation on the MIT cheetah robot,” in *Proc. IEEE Int. Conf. Robot. Autom.*, 2013, pp. 3307–3312.
- [50] T. Blackburn and K. Gaston, “Animal body size distributions: Patterns, mechanisms and implications,” *Trends Ecol. Evol.*, vol. 9, no. 12, pp. 471–474, 1994.
- [51] R. Alexander and A. Jayes, “A dynamic similarity hypothesis for the gaits of quadrupedal mammals,” *J. Zool.*, vol. 201, no. 1, pp. 135–152, 1983.
- [52] A. M. Johnson, “Gait design using self-manipulation,” in *Robotics: Science and Systems Workshop on “Dynamic Locomotion,”* Berkeley, CA, Jul. 2014.
- [53] R. Altendorfer, D. E. Koditschek, and P. Holmes, “Stability analysis of legged locomotion models by symmetry-factored return maps,” *Int. J. Robot. Res.*, vol. 23, nos. 10/11, pp. 979–999, 2004.



Thomas Libby (S'11) was born in Cleveland, TN, USA. He received the B.S. and M.S. degrees in mechanical engineering from University of California at Berkeley, Berkeley, CA, USA, in 2002 and 2012, respectively, where he is currently working toward the Ph.D. degree in mechanical engineering.

He is the Technical Director of the Center for Interdisciplinary Bio-inspiration in Education and Research, University of California at Berkeley. His research interests include comparative biomechanics and bioinspired robotics.

Mr. Libby is a member of the Society for Integrative and Comparative Biology. He was a Best Student Paper Finalist at the IEEE International Conference on Intelligent Robots and Systems, in 2011, as well as the Climbing and Walking Robots Conference in 2012.



Aaron M. Johnson (S'06–M'14) was born in Washington, DC, USA. He received the B.S. degree in electrical and computer engineering from Carnegie Mellon University, Pittsburgh, PA, USA, in 2008 and the Ph.D. degree in electrical and systems engineering from University of Pennsylvania, Philadelphia, PA, in 2014.

He is currently an Assistant Professor of mechanical engineering and robotics with Carnegie Mellon University. He was previously a Postdoctoral Fellow and Instructor with Carnegie Mellon University, a Postdoctoral Fellow with University of Pennsylvania, a Visiting Researcher with Boston Dynamics, and an Electrical Engineering Intern with iRobot. His research interests include dynamic transitions, contact-rich (self-)manipulation, bioinspired robotics, actuator modeling, and robot ethics.

Dr. Johnson is a member of the American Society of Mechanical Engineers, the Association for Computing Machinery, and the Society for Industrial and Applied Mathematics. He was a Best Student Paper Finalist at the IEEE International Conference on Robotics and Automation in 2013, as well as the Climbing and Walking Robots Conference in 2012. He received the David Thuma Laboratory Project Award in 2008 from Carnegie Mellon University and was an Honorable Mention for the Computing Research Association's Outstanding Undergraduate in 2008.



Evan Chang-Siu (S'11–M'15) was born in Vancouver, BC, Canada. He received the B.S., M.S., and Ph.D. degrees in mechanical engineering from University of California at Berkeley, Berkeley, CA, USA, in 2006, 2008, and 2013, respectively.

He is an Assistant Professor of engineering technology with California State University Maritime Academy, Vallejo, CA. His research interests include bioinspired robotics and mechatronic systems.

Dr. Chang-Siu was a Best Student Paper Finalist at the IEEE International Conference on Intelligent

Robots and Systems in 2011, as well as the Climbing and Walking Robots Conference in 2012.



Robert J. Full was born in Buffalo, NY, USA. He received the Ph.D. degree in biological science from State University of New York at Buffalo, Buffalo, in 1984.

He began a Postdoctoral position with University of Chicago in 1984. He joined the faculty of University of California at Berkeley, Berkeley, CA, USA, in 1986, where he became a full Professor of integrative biology in 1995 and currently holds a secondary appointment in electrical engineering and computer science. His research interests include motion science, neuromechanics, and bioinspired robotics.

Dr. Full is a member of the Society for Integrative and Comparative Biology.

He is currently the Editor-in-Chief of *Bioinspiration and Biomimetics*. He is a Fellow of the American Academy of Arts and Sciences and the American Association for the Advancement of Science.



Daniel E. Koditschek (S'80–M'83–SM'93–F'04) received the Ph.D. degree in electrical engineering from Yale University, New Haven, CT, USA, in 1983.

He is the Alfred Fittler Moore Professor of electrical and systems engineering with University of Pennsylvania, Philadelphia, PA, USA, where he served as the Chair from 2005 to 2012 and holds secondary appointments with the Department of Computer and Information Science and Mechanical Engineering and Applied Mechanics. Prior to joining University of Pennsylvania, he held faculty positions with the

Department of Electrical Engineering and Computer Science, University of Michigan, Ann Arbor (1993–2004) and the Department of Electrical Engineering, Yale University (1984–1992). His research interests include robotics, the application of dynamical systems theory to intelligent machines, and nonlinear control.

Dr. Koditschek is a member of the American Mathematical Society, the Association for Computing Machinery, the Mathematical Association of America, the Society for Industrial and Applied Mathematics, the Society for Integrative and Comparative Biology, and Sigma Xi. He is a Fellow of the American Association for the Advancement of Science. He received the Presidential Young Investigators Award in 1986.